DOI:
10.1115/1.4039394

Document Version
Peer reviewed version

Selective-Compliance-Based Lagrange Model and Feedback Control of a Humanoid Robot

Emmanouil Spyrakos-Papastavridis[1]
Dyson School of Design Engineering, Imperial College London, South Kensington Campus, London SW7 2AZ, UK
e.spyrakos-papastavridis@imperial.ac.uk

Jian S. Dai
Centre for Robotics Research, King's College London, Strand, London, WC2R 2LS, UK
jian.dai@kcl.ac.uk

Peter R. N. Childs
Dyson School of Design Engineering, Imperial College London, South Kensington Campus, London SW7 2AZ, UK
p.childs@imperial.ac.uk

Nikos G. Tsagarakis
Department of Advanced Robotics, Istituto Italiano di Tecnologia, via Morego, 30, 16163 Genova
nikos.tsagarakis@iit.it

ABSTRACT

This paper presents unified control schemes for compliant humanoid robots that are aimed at ensuring successful execution of both balancing tasks and walking trajectories for this class of bipeds, given the complexity of under-actuation. A set of controllers corresponding to the single support (SS) and double support (DS) walking phases has been designed based on the flexible sagittal joint dynamics of the system, accounting for both the motor and link states. The first controller uses partial state feedback (PDD), whereas the second considers the full state of the robot (PPDD), whilst both are mathematically proven to stabilize the closed-loop systems for regulation and trajectory tracking tasks. It is demonstrated mathematically that the PDD controller possesses better stability properties than the PPDD scheme for regulation tasks, even though the latter has the advantage of allowing for its associated gain-set to be generated by means of standard techniques, such as Linear Quadratic Regulator (LQR) control. A switching condition relating the Centre-of-Pressure (CoP) to the energy functions corresponding to the DS and SS models, has also been established. The theoretical results are corroborated by means of balancing and walking experiments using the COmpliant huMANoid (COMAN), whilst a practical comparison between the designed controller and a classical PD controller for compliant robots, has also been performed. Overall, and a key conclusion of this paper, the PPDD scheme has produced a significantly improved trajectory tracking performance, with 9%, 15% and 20% lower joint space error for the hip, knee and ankle respectively.

[1] Corresponding author.

1. INTRODUCTION

Bipedal robotic research has been a long-standing focus of interest in the attempt to endow robotic devices with a fundamental human capability, which consequently gave rise to a field of study aimed at systematizing the quantification of a humanoid robot's state of balance. A seminal contribution to this field of study was the introduction of the Zero-Moment-Point (ZMP) concept [1], which describes a point existing under the robot's feet whose position defines the system's overall stability. In alignment with the following premise, it is concluded that there exists a range of possible ankle torque and reaction force combinations yielding stable robot configurations, which ensures that the ZMP resides within the confines of the convex hull of the support polygon. The afore-mentioned CoP balancing criterion, which is defined based on the robot's ground-feet contact forces, has also been investigated due to its frequent equivalence with the ZMP [2]. Among the most renowned humanoids of the past two decades is the ASIMO, that has been capable of performing walking trajectories [3] using a posture control algorithm, which is an amalgamation of various schemes, such as Ground Reaction Force (GRF) control, online modification of the ZMP, and foot landing position control. An intuitive control strategy was proposed in [4], where the authors suggested five criteria that need to be satisfied in order to guarantee a biped's successful execution of a trajectory. A sensory reflex control method was presented in [5], where the robot was stabilized during a desired trajectory by performing online modification of its posture and its foot positioning. A force controller design based on a Linear Inverted Pendulum Model (LIPM), was utilized for bipedal walking [6].

When dealing with compliant humanoids, the need for more intricate control techniques is inevitable owing to the increase in the complexity of the dynamics. Even though simpler motor

PID schemes may provide tracking on stiff humanoids, this might not necessarily be the case for their compliant counterparts. Although the use of single pendulum models for developing tracking controllers [6], can lead to a reduction of the tuning complexity, these may not provide a viable solution for compliant bipeds as there is no accounting for the entirety of the state space [7]. Contrarily, full-body dynamics algorithms can be computationally cumbersome and difficult to implement [7], especially when dealing with flexible joint systems. Therefore, the method described in papers [8][9] may be viewed as a compromise between the previously described techniques, since it offers a higher degree of modelling accuracy as compared to the inverted pendulum approach, while at the same time reduces the complexity associated with the full-body dynamics of compliant humanoids.

Despite the disadvantages previously mentioned of this class of bipedal machines, their intrinsic compliance tends to enhance their impact absorption capability [10], which could augment their balancing performance, and thus there is currently a trend of shifting towards flexible machines. [11] describes the use of a dynamic, real-time trajectory that allowed the COmpliant huMANoid (COMAN) [10] to perform walking. Moreover, [12] reports on a technique of merging the inverted pendulum model with a compliant Cartesian model used to predict the Centre-Of-Mass (CoM) position and then employing Internal Model Control (IMC) to achieve the required tracking performance. The method was validated experimentally on the COMAN. [13] outlines the development of a compliant humanoid walking strategy using a combination of a posture-based state machine and a tendon-driven compliant actuator torque control scheme, to guarantee trajectory tracking.

Gravity compensation control has been the topic of several projects. [14] proposed a PD plus gravity compensation controller that has been mathematically proven to asymptotically stabilize robots composed of elastic joints. In [15], there is a description of the derivation of strict Lyapunov functions based on the energy shaping principle, which are then used to demonstrate global asymptotic stability. The approach involving the employment of full-state feedback controllers on flexible joint robots has been treated in [16]. On the other hand, [17] presented a PD plus on-line gravity compensation controller for a flexible joint that has been validated through both analytical and experimental results. Despite there being many works dealing with set-point regulation stability, consideration of trajectory tracking stability analyses for flexible joint robots are scarce. [18] provides an extensive treatment of this topic, while managing to prove local exponential stability when considering an array of PD controllers for these systems. [19] demonstrated that semi-global asymptotical tracking stability was achievable for these systems when considering full-state feedback, although the dynamical models considered in the work neglected the presence of damping elements on both the motor and link sides. It is worth noting however that [20] proves global asymptotic tracking stability for several compliant joint robot controllers, employing link and torque (constructed using the deflection magnitude) feedback, even though it has been stated [16] that the implementation of the proposed controllers on real systems is demanding, due to the model uncertainties and the associated difficulties in interpreting and debugging the results.

This paper expands on the afore-mentioned work by means of providing trajectory tracking stability proofs for equal-actuated and over-actuated gravity compensation controllers, employing motor position, motor velocity and link velocity feedback (PDD control), while also

including link and motor damping in the dynamical models. To elaborate, the inclusion of link velocity feedback increases the dimensions of the motor PD plus gravity compensation controllers and hence allows for the attainment of higher bandwidths, while the global asymptotic stability property of the closed-loop system is preserved. The work seen in [16] considers full-state feedback control, involving a control signal that is constituted of motor position and velocity, in addition to torque and torque derivative feedback, while the scheme's capability of stable set-point regulation is also proven. A similar control technique employing full-state feedback is proposed here, namely the PPDD plus gravity compensation controller, whose gains are designed using decentralized LQR methods, and an accompanying set of tracking stability proofs is provided.

This paper's tracking results are valuable since stability analyses for bipedal robot (and especially for compliant humanoid) controllers are somewhat uncommon in the literature. One of these cases is seen in [21], where Input-to-State Stability (ISS) has been demonstrated for a particular bipedal robot controller, based on a simple model. Additionally, asymptotical stability for a class of under-actuated, bipedal walkers, has been demonstrated in [22][23], by means of Poincaré maps.

Full-body gravity compensation control of humanoids was initially presented in [24] and proved to be an apt choice as far as the execution of dynamical tasks was concerned. However, [25] proposed the use of virtual gravity compensation torque control for the development of a balance controller capable of attaining natural bipedal walking. A method by which the GRFs can be translated into joint torques is described by [26], mathematically proving this specific controller's passivity.

The method proposed in this paper is an extension to the work seen in [9], which involves the use of PDD control (motor position, motor velocity and link velocity feedback) on 6 degree-of-freedom (DOF) SS and 3-DOF DS models of the robot, in combination with gravity compensation control. The mathematical models describe the full compliant dynamics (the motor and link dynamics appearing before and after the elastic element), thereby accounting for the mere sagittal elements, since it is only those joints that comprise Series Elastic Actuators (SEA). Conversely, the robot's lateral joints may be regarded as being structurally 'stiff', thereby rendering a flexible-joint-based mathematical representation unnecessary. Furthermore, the joint controllers function by utilising position and velocity feedback control, while a state machine is used to switch between the three distinct models as well as between the three different gravity vectors. In comparison to [9], this paper demonstrates that the proposed controller is capable of offering closed-loop tracking stability and that the whole system is actually stable, considering the switching between the DS and SS models and controllers during walking.

The rest of the paper is structured as follows. Section 2 introduces the over-actuated [27] and equal-actuated dynamical models, Section 3 delineates the PDD and full-state (PPDD), plus gravity compensation control schemes, while Section 4 provides their associated theoretical stability proofs, in addition to the controller switching approach. Section 5 addresses the steps involved in tuning the controllers in simulation and their practical implementation, together with the pertinent experimental and controller comparison results provided in Section 6. Finally, conclusions are discussed in Section 7, followed by appendices including the tracking stability analyses and an array of bounded terms.

2. SELECTIVE COMPLIANCE-BASED LAGRANGE MODEL WITH AN OVER-ACTUATED SCHEME

This section delineates the SS and DS dynamics of a humanoid powered by compliant actuators. In order to model the equal-actuated SS phase, in which the number of link DoFs equals the number of actuators, a generic n-DoF robot possessing n drives is considered, whose link dynamics is described by the following equation [28]:

$$\mathbf{M_J}(\boldsymbol{q})\ddot{\boldsymbol{q}} + \mathbf{N}\dot{\boldsymbol{q}} + \mathbf{C}(\boldsymbol{q}, \dot{\boldsymbol{q}})\dot{\boldsymbol{q}} + \mathbf{P}\boldsymbol{q} - \mathbf{P}\boldsymbol{\theta} = \boldsymbol{\tau_g}(\boldsymbol{q}), \tag{1}$$

whereas its motor dynamics is represented as follows [28]:

$$\mathbf{J}\ddot{\boldsymbol{\theta}} + \mathbf{D}\dot{\boldsymbol{\theta}} - \mathbf{P}\boldsymbol{q} + \mathbf{P}\boldsymbol{\theta} = \mathbf{K_{VT}}\boldsymbol{V_m}, \tag{2}$$

with the elastic terms providing the coupling between the two formulae. Additionally, $\boldsymbol{q}$ and $\boldsymbol{\theta}$ represent the link and motor positions, while $\mathbf{M_J}(\boldsymbol{q})$, $\mathbf{N} \in \mathbb{R}^{n\times n}$ are the symmetric inertia matrix and the diagonal damping matrix, $\mathbf{C}(\boldsymbol{q}, \dot{\boldsymbol{q}}) \in \mathbb{R}^{n\times n}$ is the skew-symmetric Coriolis/centripetal matrix, $\boldsymbol{\tau_g}(\boldsymbol{q}) \in \mathbb{R}^n$ is the gravitational torque vector, $\mathbf{K_{VT}} \in \mathbb{R}^{n\times n}$ is the diagonal voltage-to-torque gain matrix and $\boldsymbol{V_m} \in \mathbb{R}^n$ denotes the motor voltages. $\mathbf{P} \in \mathbb{R}^{n\times n}$ is a diagonal matrix with positive entries signifying the passive spring stiffness between the motors and the robot links, while $\mathbf{J}, \mathbf{D} \in \mathbb{R}^{n\times n}$ are the diagonal motor inertia and damping. Additionally, the DS phase is modelled using a $j = 3$-DOF robot with $n = 2$ drives for each DOF, where the total number of drives is $n \times j = 6$. Therefore, the associated dynamics can be represented as follows [8]:

$$\mathbf{M_{J0}}(\boldsymbol{q_0})\ddot{\boldsymbol{q}}_\mathbf{0} + \mathbf{N_0}\dot{\boldsymbol{q}}_\mathbf{0} + \mathbf{C_0}(\boldsymbol{q_0}, \dot{\boldsymbol{q}}_\mathbf{0})\dot{\boldsymbol{q}}_\mathbf{0} + \mathbf{S_m^T}\mathbf{P}(\mathbf{S_m}\boldsymbol{q_0} - \boldsymbol{\theta}) = \boldsymbol{\tau}_{\boldsymbol{g0}}(\boldsymbol{q_0}), \tag{3}$$

$$\mathbf{J}\ddot{\boldsymbol{\theta}} + \mathbf{D}\dot{\boldsymbol{\theta}} - \mathbf{P}\mathbf{S_m}\boldsymbol{q_0} + \mathbf{P}\boldsymbol{\theta} = \mathbf{K_{VT}}\boldsymbol{V_{m0}}, \tag{4}$$

where $\boldsymbol{q_0}$ is a vector representing the DS system's link positions, $\mathbf{M_{J0}}(\boldsymbol{q_0})$, $\mathbf{N_0}$ and $\mathbf{C_0}(\boldsymbol{q_0}, \dot{\boldsymbol{q}}_0) \in \mathbb{R}^{j\times j}$, $\boldsymbol{V_{m0}} \in \mathbb{R}^n$, and $\boldsymbol{\tau_{g0}}(\boldsymbol{q_0}) \in \mathbb{R}^j$ are the DS phase's counterparts of $\mathbf{M_J}(\boldsymbol{q})$, $\mathbf{N}$, $\mathbf{C}(\boldsymbol{q}, \dot{\boldsymbol{q}})$, $\boldsymbol{V_m}$ and $\boldsymbol{\tau_g}(\boldsymbol{q})$ respectively. Furthermore, $\mathbf{S_m^T} \in \mathbb{R}^{j\times n}$ is an assignment matrix describing the over-actuation by means of assigning two motors to every link, and is therefore composed of ones and zeros, with its columns associated to the system's motors and its rows to the system's joints. Arranging the motor equation so that the first n_1 drives are connected to link 1, the next n_2 are connected to link 2 and so on, then $\mathbf{S_m^T}$ is given as follows:

$$\mathbf{S_m^T} = \begin{bmatrix} \underbrace{1 \cdots 1}_{n_1} & 0 \cdots 0 & \cdots & 0 \cdots 0 \\ 0 \cdots 0 & \underbrace{1 \cdots 1}_{n_2} & \cdots & 0 \cdots 0 \\ \vdots & \vdots & \ddots & \vdots \\ 0 \cdots 0 & 0 \cdots 0 & \cdots & \underbrace{1 \cdots 1}_{n_j} \end{bmatrix}. \tag{5}$$

Similar cases of over-actuation, as well as more extreme ones involving 10 drives per DoF, are ubiquitous in biomechanics literature [29]. In order to maintain an adequate degree of accuracy when mathematically describing the robot, it was essential to include all the sagittal joints in the system's model. This could be seen as an improvement when compared to employing an inverted pendulum model, while it also dispenses with the need for full-body dynamics. 6-DOF models (Fig. 1) were used to represent the SS phases, while a 3-DOF model (Fig. 1) was employed for the modelling of the DS phase. Fig. 1 also depicts the left and right GRFs F_{Z_L} and F_{Z_R}. The gravity vectors differed significantly between the SS and DS phases and hence had to be computed independently. The entries of the 6-DOF SS vectors were arranged as follows:

$$\boldsymbol{\tau_g} = [\tau_{sa} \quad \tau_{sk} \quad \tau_{sh} \quad \tau_{sw} \quad \tau_{swk} \quad \tau_{swa}]^T,$$

with $\tau_{sa}, \tau_{sk}, \tau_{sh}, \tau_{swh}, \tau_{swk}, \tau_{swa}$ being the support ankle, knee and hip, and swing hip, knee and ankle torques respectively. On the other hand, the elements of the 3-DOF DS vector were ordered as follows:

$$\boldsymbol{\tau_{g0}} = [\tau_a \quad \tau_k \quad \tau_h]^T,$$

with τ_a, τ_k, τ_h representing the ankle, knee and hip torques respectively. An important property of the gravity vector is the following [30]:

$$\left\| \frac{\partial \boldsymbol{\tau_g}(\boldsymbol{q})}{\partial \boldsymbol{q}} \right\| = \left\| \frac{\partial^2 U_g(\boldsymbol{q})}{\partial \boldsymbol{q^2}} \right\| \leq \alpha, \tag{6}$$

for some $\alpha > 0$; here $U_g(\boldsymbol{q})$ denotes the potential energy due to gravity, and $\boldsymbol{\tau_g}(\boldsymbol{q}) = -\left(\partial U_g(\boldsymbol{q})/\partial \boldsymbol{q}\right)^T$. A similar expression holds for the DS model gravity vector $\boldsymbol{\tau_{g0}}(\boldsymbol{q_0})$. Three dynamical models were used in total to model the various phases of the walking trajectory.

Table I summarizes the above models with LSS, RSS and DS standing for 'left single support', 'right single support', and 'double support' respectively. This approach resulted in the attainment of a set of mathematical models that provided a closer approximation to the non-linear nature of the robot's dynamics when switching between the various phases of a walking trajectory, as opposed to using a single model during the whole trajectory. It is noteworthy that the joints comprising the DS model are not constrained to being completely coaxial, since the model has demonstrated robustness to deviations, with respect to the upright stance.

TABLE I
DYNAMICAL MODELS

Model	DOF's
DS	3
LSS	6
RSS	6

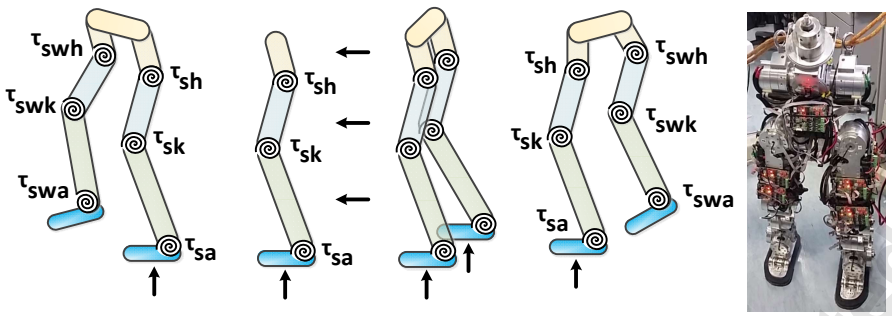

Figure 1. LSS (left), DS (centre) and RSS (right) models, and picture of COMAN's legs (rightmost).

3. GRAVITY COMPENSATION CONTROLLERS WITH LINK VELOCITY AND LINK POSITION AUGMENTED FEEDBACK

3.1 Gravity Compensation Controller with Link Velocity Feedback

The controller design attempts to eliminate the gravitational effects present in the system so as to ensure global stability of the closed-loop, while it utilizes link velocity feedback for the purpose of enhancing the damping performance on the link side. The controller utilised for the compliant humanoid system, (1), and its associated motor dynamics, (2), is described via the following PDD control law:

$$\boldsymbol{V_m} = \mathbf{K_{m1}}(\boldsymbol{q_d} - \boldsymbol{\theta}) - \mathbf{K_{m2}}\dot{\boldsymbol{\theta}} - \mathbf{K_{j2}}\dot{\boldsymbol{q}} + \boldsymbol{u_{gc}}, \tag{7}$$

where $\boldsymbol{u_{gc}} \in \mathbb{R}^n$ is the gravity compensation term and $\boldsymbol{q_d}$ is the desired link position, $\mathbf{K_{m1}}$, $\mathbf{K_{m2}} \in \mathbb{R}^{n\times n}$ are the diagonal, positive definite motor position and motor velocity feedback gain matrices corresponding to the SS system, while a link velocity gain, $\mathbf{K_{j2}} \in \mathbb{R}^{n\times n}$, is also introduced.

For the SS phase, if one sets $\dot{\boldsymbol{q}}, \dot{\boldsymbol{\theta}} = 0$ in equations 1, 2 and 7, then $\boldsymbol{u_{gc}}$ is given by:

$$\boldsymbol{u_{gc}} = -\mathbf{K_{VT}^{-1}} \cdot (\mathbf{K_{VT}}\mathbf{K_{m1}}\mathbf{P^{-1}} + \mathbf{I}) \cdot \boldsymbol{\tau_g}(\boldsymbol{q_d}). \tag{8}$$

The overall stiffness matrix corresponding to the SS phase, is the following:

$$\mathbf{T_S} = \begin{bmatrix} \mathbf{P} & -\mathbf{P} \\ -\mathbf{P} & \mathbf{K_{VT}K_{m1}} + \mathbf{P} \end{bmatrix}, \tag{9}$$

and has been defined separately for use in the subsequent section. Moreover, $\boldsymbol{\theta_d}$ is defined as:

$$\boldsymbol{\theta_d} = \boldsymbol{q_d} - \mathbf{P^{-1}}\boldsymbol{\tau_g}(\boldsymbol{q_d}). \tag{10}$$

The control law for the DS system is similar to its SS counterpart, although in this case an assignment matrix, $\mathbf{S_m}$, is introduced to assure that the appropriate link elements are considered, as shown below:

$$\boldsymbol{V_{m0}} = \mathbf{K_{m1_0}}\left(\mathbf{S_m}\boldsymbol{q_{0_d}} - \boldsymbol{\theta}\right) - \mathbf{K_{m2_0}}\dot{\boldsymbol{\theta}} - \mathbf{K_{j2_0}}\dot{\boldsymbol{q}}_{\mathbf{0}} + \boldsymbol{u_{gc_0}}, \tag{11}$$

with $\mathbf{K_{m1_0}}$, $\mathbf{K_{m2_0}}$ and $\mathbf{K_{j2_0}}$ being the DS system's gain matrices and $\boldsymbol{q_{0_d}}$ being the desired link position. For the DS, $\boldsymbol{u_{gc_0}}$ is given by:

$$\boldsymbol{u_{gc_0}} = -\mathbf{K_{VT}^{-1}}\left(\mathbf{K_{VT}K_{m1_0}P^{-1}} + \mathbf{I}\right)(\mathbf{S_m^T})^{+}\boldsymbol{\tau_{g0}}\left(\boldsymbol{q_{0_d}}\right), \tag{12}$$

where $(\mathbf{S_m^T})^{+}$ denotes the Moore-Penrose pseudoinverse of $\mathbf{S_m^T}$. The DS total stiffness, $\mathbf{T_D}$, is defined as:

$$\mathbf{T_D} = \begin{bmatrix} \mathbf{S_m^T P S_m} & -\mathbf{S_m^T P} \\ -\mathbf{P S_m} & \mathbf{K_{VT}K_{m1_0}} + \mathbf{P} \end{bmatrix}. \tag{13}$$

Additionally, for the DS:

$$\boldsymbol{\theta_d} = \mathbf{S_m}\boldsymbol{q_{0_d}} - \mathbf{P^{-1}}(\mathbf{S_m^T})^{+}\boldsymbol{\tau_{g0}}\left(\boldsymbol{q_{0_d}}\right). \tag{14}$$

Two additional matrices composed of dissipative elements, are also provided:

$$\boldsymbol{\gamma} = \mathbf{N} \cdot (\mathbf{D} + \mathbf{K_{VT}K_{m2}}) - \frac{\left(\mathbf{K_{VT}K_{j2}}\right)^2}{4}, \tag{15}$$

$$\boldsymbol{\gamma_0} = \mathbf{N_0} \cdot \left(\mathbf{D} + \mathbf{K_{VT}K_{m2_0}}\right) - \frac{\left(\mathbf{K_{VT}K_{j2_0}}\right)^2}{4}, \tag{16}$$

that are to be used together with the $\mathbf{T_S}$ and $\mathbf{T_D}$ matrices in the stability analyses.

3.2 Link-Position-Augmented Gravity Compensation Control Using the Linear Quadratic Regulator Approach

One could elect to augment the dimension of the previously described controller through the addition of link position feedback, thus yielding the following PPDD control law:

$$\boldsymbol{V_m = -\mathbf{K_{j1}} q - \mathbf{K_{m1}} \theta - \mathbf{K_{j2}} \dot{q} - \mathbf{K_{m2}} \dot{\theta} + \mathbf{G_{ff}} q_d + u_{gc},} \qquad (\mathbf{17})$$

wherein $\mathbf{G_{ff}} = \mathbf{K_{j1}} + \mathbf{K_{m1}}$. This should theoretically increase the closed-loop system's bandwidth, although it would lead to complications with the resulting/associated stability proofs. It is worth noting that by carrying out an analogous stability analysis to that presented in Appendix C, the above controller is shown to result in an ISS (abbreviation defined in the Introduction section, explanation provided in [31]) system for trajectory tracking. This clearly undermines the PPDD controller's value as regards regulation tasks, since it relates to a feebler stability condition than that attained for the PDD controller. Nevertheless, the introduction of decentralized full-state (PPDD) feedback drastically enhances the pertinent controller's practical value, since its associated PPDD gains could be generated by means of a standard, well-established method, such as LQR control. Using the dynamical equations $(1) - (4)$ presented earlier, the system is linearized about the desired configurations in accordance with the trajectory data and the technique described in [32]. Using the latter approach, the Coriolis and centrifugal terms disappear, and the system is solved with respect to the accelerations, thereby requiring an inversion of the inertia matrix. This yields a set of three linearized models, which may be represented in the following generic state-space form:

$$\begin{bmatrix} \dot{\boldsymbol{q}} \\ \dot{\boldsymbol{\theta}} \\ \ddot{\boldsymbol{q}} \\ \ddot{\boldsymbol{\theta}} \end{bmatrix} = \begin{bmatrix} \mathbf{0} & \mathbf{I} \\ -\mathbf{M_L^{-1}P_L} & -\mathbf{M_L^{-1}N_L} \end{bmatrix} \begin{bmatrix} \boldsymbol{q} \\ \boldsymbol{\theta} \\ \dot{\boldsymbol{q}} \\ \dot{\boldsymbol{\theta}} \end{bmatrix} + \begin{bmatrix} \mathbf{0} \\ \mathbf{M_L^{-1}E_m K_{VT}} \end{bmatrix} \boldsymbol{u}, \tag{18}$$

where $\mathbf{E_m} \in \mathbb{R}^{2n \times n}$ is a selection matrix, while $\mathbf{M_L} \in \mathbb{R}^{2n \times 2n}$, $\mathbf{P_L} \in \mathbb{R}^{2n \times 2n}$ and $\mathbf{N_L} \in \mathbb{R}^{2n \times 2n}$ denote the linearized motor and link inertia, stiffness, and damping matrices respectively. Alternatively, the above equation could be described in a succinct manner as follows:

$$\dot{\boldsymbol{x}} = \mathbf{A}\boldsymbol{x} + \mathbf{B}\boldsymbol{u}, \tag{19}$$

with $\mathbf{A} \in \mathbb{R}^{4n \times 4n}$, $\mathbf{B} \in \mathbb{R}^{4n \times n}$, $\boldsymbol{u} = -\mathbf{K_{LQR}}\boldsymbol{x}$, and $\mathbf{K_{LQR}} \in \mathbb{R}^{n \times 4n}$ being the set of generic PPDD gains generated by minimizing the cost function J_{LQR}, subject to the model's dynamics, as shown below:

$$J_{LQR} = \int_0^{\infty} (\boldsymbol{x}^T \mathbf{Q} \boldsymbol{x} + \boldsymbol{u}^T \mathbf{R} \boldsymbol{u})\, dt. \tag{20}$$

In order to describe the walking phases, it is evident that three such systems are required, and these may be expressed via the following equations:

$$\dot{\boldsymbol{x}}_{\boldsymbol{LS}} = \mathbf{A_{LS}}\boldsymbol{x}_{\boldsymbol{LS}} + \mathbf{B_{LS}}\boldsymbol{u}_{\boldsymbol{LS}},$$

$$\dot{\boldsymbol{x}}_{\boldsymbol{RS}} = \mathbf{A_{RS}}\boldsymbol{x}_{\boldsymbol{RS}} + \mathbf{B_{RS}}\boldsymbol{u}_{\boldsymbol{RS}},$$

$$\dot{\boldsymbol{x}}_{\boldsymbol{DS}} = \mathbf{A_{DS}}\boldsymbol{x}_{\boldsymbol{DS}} + \mathbf{B_{DS}}\boldsymbol{u}_{\boldsymbol{DS}},$$

corresponding to the LSS, RSS and DS phases, with $\mathbf{A_{LS}} \in \mathbb{R}^{4n \times 4n}$, $\mathbf{B_{LS}} \in \mathbb{R}^{4n \times n}$, $\mathbf{A_{RS}} \in \mathbb{R}^{4n \times 4n}$, $\mathbf{B_{RS}} \in \mathbb{R}^{4n \times n}$, $\mathbf{A_{DS}} \in \mathbb{R}^{2(j+n) \times 2(j+n)}$, $\mathbf{B_{DS}} \in \mathbb{R}^{2(j+n) \times n}$ which possess the $\mathbf{K_{LQR_L}} \in \mathbb{R}^{n \times 4n}$, $\mathbf{K_{LQR_R}} \in \mathbb{R}^{n \times 4n}$ and $\mathbf{K_{LQR_D}} \in \mathbb{R}^{n \times 2(j+n)}$ gain matrices respectively. It is worth noting that the centralized controller obtained using equation (20), was transformed into a decentralized one by following the procedures outlined in [33][34], thus producing a set of diagonal and symmetric gain matrices. The above formulae initially exclude the gravitational effects, although these shall

be accounted for via the addition of the gravity compensation terms, yielding the control law described by equation (17). An important matrix to be defined for this specific controller, is the following:

$$\mathbf{T_{S_{LQR}}} = \begin{bmatrix} \mathbf{P} & -\mathbf{P} \\ \mathbf{K_{VT}K_{j1}} - \mathbf{P} & \mathbf{K_{VT}K_{m1}} + \mathbf{P} \end{bmatrix}, \tag{21}$$

which is essential for the tracking stability analysis that was referred to earlier and is clearly outlined in Appendix C. A similar condition to (15) needs to be satisfied by equation (21), in order to ensure its positive definiteness, and this can be described as $\lambda_{min}(\boldsymbol{\gamma_{LQR}}) > 0$, for which $\mathbf{W} = \mathbf{P}$, $\mathbf{X} = -\mathbf{P}$, $\mathbf{Y} = \mathbf{K_{VT}K_{j1}} - \mathbf{P}$ and $\mathbf{Z} = \mathbf{K_{VT}K_{m1}} + \mathbf{P}$.

4. SET-POINT REGULATION AND TRACKING STABILITY ANALYSES

This section outlines the theorems for the closed-loop stability results. In view of the fact that this work has focused on both set-point regulation, and trajectory tracking proofs and experiments, the relevant theorems pertaining to either class of results, are demarcated by the two subsequent subsections.

4.1 Single and Double Support Stability using LaSalle's Principle and the Assignment Matrix

For the purpose of proving the closed-loop stability of both the SS and DS controllers, it was essential that the $\mathbf{T_S}$, $\mathbf{T_D}$, $\boldsymbol{\gamma}$ and $\boldsymbol{\gamma_0}$ matrices satisfied certain inequalities, as stipulated by the theorem statements provided below:

Theorem 1: If the minimum eigenvalues $\lambda_{\min}(\mathbf{T_S}) > \alpha$ and $\lambda_{\min}(\boldsymbol{\gamma}) > 0$, then there is a unique equilibrium solution $[\boldsymbol{q_d^T} \quad \boldsymbol{\theta_d^T} \quad 0 \quad 0]^{\mathrm{T}}$ that is globally asymptotically stable.

Theorem 2: If $\lambda_{min}(\mathbf{T_D}) > \alpha$ and $\lambda_{min}(\boldsymbol{\gamma_0}) > 0$, then there is a unique equilibrium solution $\begin{bmatrix} \boldsymbol{q_{0_d}^T} & \boldsymbol{\theta_{0_d}^T} & 0 & 0 \end{bmatrix}^T$, that is globally asymptotically stable.

The accompanying stability analyses, namely Proof 1 and Proof 2, are delineated in Appendix B, demonstrating that the main discrepancy between the two analyses is associated with the dimensions of the vectors and matrices that relate to each controller.

4.2 Tracking Stability of the Full-State Feedback Controller

The stability analyses presented in the previous sub-section only attest to the closed-loop system's stability when using set-point references, which makes them useful for balance recovery applications. However, during bipedal walking, a set of time-varying references are fed to the robot, thus reducing the relevance of these results. For this reason, a tracking stability analysis is presented in Appendix C, based on the work seen in [18], demonstrating that the robot can track time-varying references in a stable manner in both DS and SS. It is noteworthy that this section initially considers the stability of the full-state PPDD controller described by equation (17), through Theorems 4 and 5, and utilizes these results as a substratum to prove tracking stability for the reduced-dimension PDD controller, as stated in Theorems 6 and 7. The intermediate results provided by Theorem 3 and Proof 3, found in Appendix C, lay the foundations for the formulation of Theorems 4 and 5, described below:

Theorem 4: Using the controller described by equation (17) on the LSS and RSS models, while assuming an adequately small $\eta_{q_d} = sup\left\|\dot{\boldsymbol{q}}_{\boldsymbol{F_d}}(t)\right\|$ value and that $\lambda_{min}\left(\boldsymbol{\gamma}_{\mathbf{LQR_{SS}}}\right) > 0$, then the

closed-loop system is Lagrange stable.

It should be noted that the notion of Lagrange stability pertains to the uniform boundedness and uniform ultimate boundedness of dynamical systems, as described extensively in [31].

Theorem 5: Using the DS counterpart of the controller described by equation (17), on the DS model, while assuming an adequately small $\eta_{q_d} = sup\left\|\dot{\boldsymbol{q}}_{\boldsymbol{F_d}}(t)\right\|$ value and that $\lambda_{min}\left(\boldsymbol{\gamma}_{\mathbf{LQR_{DS}}}\right) > 0$, then the closed-loop system is ISS.

The associated proofs, see Appendix C, prove Lagrange stability of the closed-loop system when supplied with time-varying references, which is a weaker condition than global asymptotic stability that had been demonstrated for the set-point regulation tasks. Nevertheless, these results accomplish the task of providing a stability proof [35] for this class of full-state (PPDD) feedback plus gravity compensation controllers for compliant robots [36][37].

It is occasionally deemed redundant to derive and present the theoretical regulation stability results, as was performed in the previous subsections, if tracking stability has already been established, since the latter tacitly attests to set-point stability. However, the regulation results exhibit a stronger stability condition, namely global asymptotic stability, as opposed to Lagrange stability for the tracking tasks. Moreover, the conditions accompanying the regulation proofs are rather lenient and less involved than those related to the tracking proofs, which implies that if one were to implement the described controllers to perform a standing balance task revolving solely around the provision of set-point references, it would be less intricate to corroborate or ensure the closed-loop system's stability, in contrast to undergoing a similar procedure for the execution of a walking task.

4.3 Force Feedback Utilisation for On-Line Stabilised Switching

Even though it was previously proven that the individual closed-loop systems are capable of tracking time-varying reference signals, the stability of the overall system has hitherto been omitted from the analysis. In order to ensure the full system's stability, the time derivatives of the Lyapunov functions (a description of Lyapunov functions is provided in [38]) associated with each subsystem should be negative definite at all times, which has shown to be true for the SS model in Appendix C, while an analogous analysis allows for the attainment of equivalent results for the DS model. A satisfaction of the above conditions would imply that:

$$\begin{aligned} V_{TS}(t) &\leq e^{-\Phi_{VS1}(t-t_0)}\left[V_{TS}(t_0) - \frac{\Phi_{VS}}{\Phi_{VS1}}\right] + \frac{\Phi_{VS2}}{\Phi_{VS1}}, \\ V_{TD}(t) &\leq e^{-\Phi_{VS3}(t-t_0)}\left[V_{TD}(t_0) - \frac{\Phi_{VS4}}{\Phi_{VS}}\right] + \frac{\Phi_{VS}}{\Phi_{VS3}}, \end{aligned} \tag{22}$$

$$\begin{aligned} \dot{V}_{TD} &\leq -\Phi_{VD}\ e^{-\Phi_{VD}\ (t-t_0)}, \\ \dot{V}_{TS} &\leq -\Phi_{VS}\ e^{-\Phi_{VS1}(t-t_0)}, \end{aligned} \tag{23}$$

where V_{TD}, V_{TS}, $\dot{V}_{TD}$ and $\dot{V}_{TS}$ (defined in Appendix C) are the Lyapunov functions and Lyapunov function derivatives of the DS model with DS gains and the SS model with SS gains respectively, t and t_0 denote the time and initial time respectively, while the terms Φ_{VS1}, Φ_{VS2}, Φ_{VS3}, Φ_{VS4}, Φ_{VD1} are explicitly defined in Appendix C. The theorem introduced in [39] assumes that the controller and model switching are perfectly synchronized, and therefore the same assumption is made herein. If condition (8) shown in [39], is satisfied, then the switched system is stable. However, a prerequisite for stability is that the individual models are valid at any given point in time, which is of course dependent upon whether or not the system's X_{CoP} resides within the support polygon. The concept is that given an ideal, trajectory-defined switching time, a bound on the CoP (or the ZMP) velocity, and a distance from the CoP (or the ZMP) to the edge of the

polygon, then a condition on the controller switching time can be derived. Therefore, an additional criterion guaranteeing the X_{CoP}'s confinement within the limits of the support polygon, can be developed by firstly considering the distance from the X_{CoP} to the edge of the support polygon:

$$d(X_{CoP}, \varepsilon_{EDGE}) \leq \varepsilon, \tag{24}$$

with ε being a positive constant. Additionally, it can be assumed that the CoP velocity is bounded such that:

$$\left|\dot{X}_{CoP}\right| \leq v_{CoP}, \tag{25}$$

where v_{CoP} is a positive constant, while it can also be assumed that there is a finite difference between the ideal, trajectory-defined switching time, t_d, and the actual switching time, t_{switc} :

$$|t_{switc} - t_d| \leq t_s, \tag{26}$$

wherein t_s is a positive variable. Having defined all the required bounded terms, the switching condition may now be stated:

$$t_s \cdot v_{CoP} < \alpha_{CoP} \cdot \varepsilon, \tag{27}$$

where the $0 < \alpha_{CoP} < 1$ variable has been introduced to allow for a tuning of the condition's conservativeness. This condition must obviously be respected during every DS to SS, and during every SS to DS switch that could possibly transpire over the course of the trajectory. In other words, if the t_{swit} value at any given point in time leads to a satisfaction of both condition (8) in [39], and (22), then the walking system is stable.

Alternative methodologies for the assessment and control of a compliant humanoid's balance in real time, have been delineated in [40]-[42].

5 CONTROLLER TUNING AND IMPLEMENTATION

In terms of specifications, the COMAN's lower body comprises 15 DOFs that form a structure standing at a height of 790 mm and weighing 17.28 kg. Of these 15 DOFs, it is only the 6 pertaining to the sagittal joints that are powered by series elastic actuators, while the remaining 9 are devoid of such elements. Each sagittal compliant joint incorporates three position sensors and a torque sensor, in addition to 6-axis Force/Torque (FT) sensors at the ankles. Table II provides a painstaking listing of the system's link inertia, mass, and length parameters.

TABLE II
LEG PARAMETER VALUES

Link	Mass (kg)	Inertia Tensor $(kg \cdot m^2)$	Length (m)
Upper Body	5.54	diag(0.0253, 0.0085, 0.0216)	0.301
Thigh	2*2.77	diag(0.0144, 0.0144, 0.0007)	0.226
Lower Leg	2*2.47	diag(0.0154, 0.0148, 0.0012)	0.201
Foot	2*0.63	diag(0.0005, 0.0012, 0.0009)	0.062

5.1 Regulation and Balancing Experiments

The PDD plus gravity compensation controller was selected for the performance of these balancing experiments, since it is the one that conforms most closely with the pertinent theory, given that it yields a globally asymptotically stable closed-loop system for regulation tasks. Performing these balancing tests was a crucial part of the controller validation process as they provided an intuitive means of assessing the resemblance of the real results with those produced in simulation. During these experiments, the robot was placed on the floor in a DS stance. Fig. 2 depicts the ankle, knee and hip simulation responses whereas Fig. 3 shows the corresponding experimental responses to referential input position steps of 0.3 radians, which were fed to all the sagittal joints simultaneously.

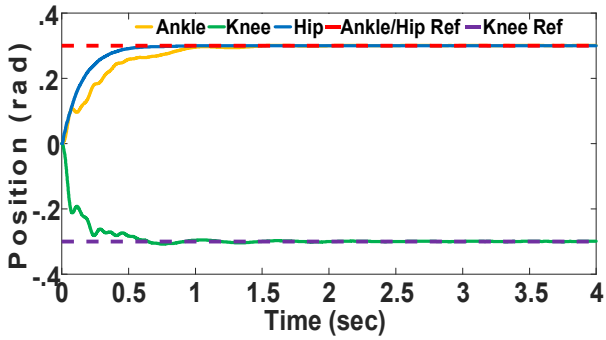

Figure 2. Simulated joint responses (0.3 radians step).

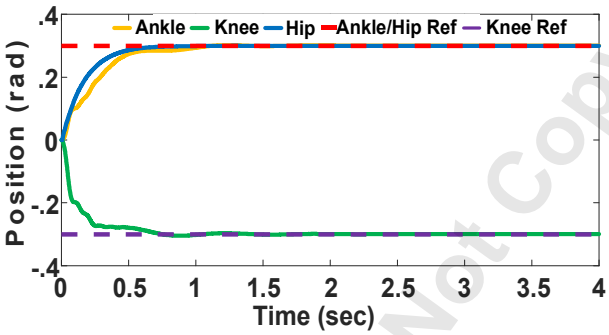

Figure 3. Actual joint responses (0.3 radians step).

It is evident that the simulation results display higher levels of oscillations in both the transient and steady-state responses. This is one means of determining the level of precision that the simulated model bears with respect to the actual system, and minor discrepancies shall inevitably exist, thus highlighting a slight degree of imprecision in certain parameter values. The existence of such discrepancies could be attributed to the nature of the developed friction models, since the temperature and time dependency of the dynamical terms, renders their accurate modelling an onerous task. Contrarily, the work presented here accounts solely for the motor damping and link friction terms, whose values are presented in Table III, whilst neglecting other relevant frictional terms, such as Stribeck friction.

TABLE III
DAMPING PARAMETER VALUES

Joint	Motor Damping $\left(\frac{N\,m\cdot s}{rad}\right)$	Link Friction $\left(\frac{N\,m\cdot s}{rad}\right)$
Ankle	0.1387	1.2
Knee	0.1387	0.2
Hip	0.1387	1.1

The controller's robustness was scrutinized by means of applying disturbances to the robot while it was assuming a DS stance. The FT sensors embedded in the robot's feet were used for an online estimation of the CoP position, while the desired CoP position was set to zero, which was located at a point that was 90 mm and 50 mm away from the positive frontmost and negative rearmost limits of the support polygon respectively. It has been assumed that the robot's feet are rectangular, while the support polygon's length in the frontal plane (x direction) is 140 mm when the robot's feet in the DS stance are completely parallel to each other, as depicted in Fig.4.

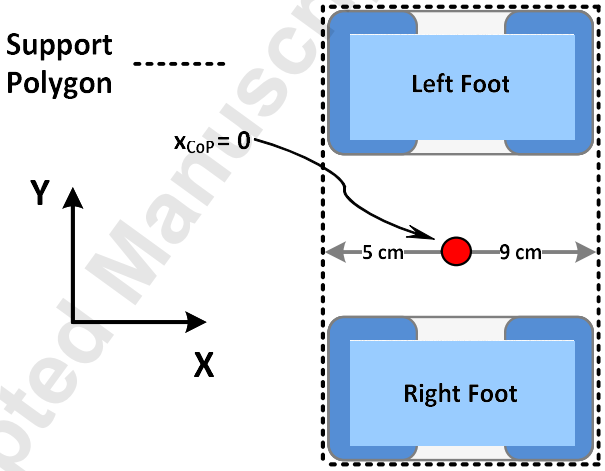

Figure 4. Support polygon shape corresponding to DS stance.

Fig. 5 portrays the stabilization scheme's capability of damping out the oscillations caused by the external perturbations applied onto the robot's structure, by means of human-induced manual exertions. To achieve this experimental setup, the robot was positioned on the floor in a DS

stance, whilst a human perturbed its structure in a bimanual fashion. Therefore, the robot's balance recovery function was assigned exclusively to the balancing controller as human intervention was prohibited during the course of the experiment. In a practical sense this meant that the robot's body returned to the zero position after a finite time period following the disturbance application. The magnitude of the perturbations was assessed through the monitoring of the robot's initial velocity value that instantly ensued the disturbance. The robot was subjected to external force perturbations ranging between 5 and 25 N, conducing to initial CoM velocities of approximately 0.2-0.6 m/sec, which it was capable of withstanding in a stable fashion. It is noteworthy that the robot was pushed solely from the rear as the support area is larger at the front.

Despite presenting the theory behind the controller's stability in Appendix B, it must now be proven that the designed controllers satisfy not only conditions $\lambda_{\min}(\mathbf{T_S}) > \alpha$ and $\lambda_{\min}(\boldsymbol{\gamma}) > 0$, but also conditions $\lambda_{\min}(\mathbf{T_D}) > \alpha$ and $\lambda_{\min}(\boldsymbol{\gamma_0}) > 0$. From a theoretical point of view, the stability analyses allow us to conclude global stabilization for each distinct model, using our proposed controller. In practice however, such an assumption might not always be valid and can be verified numerically. Thus, the aim is to obtain a bound for the gravity vector derivative, represented by the constant α in (6), through the insertion of the physical joint angle limits into the LHS of (6). Table IV lists the minimum eigenvalues, $\lambda_{\min}(\mathbf{T_D})$, $\lambda_{\min}(\mathbf{T_S})$, $\lambda_{\min}(\boldsymbol{\gamma_0})$ and $\lambda_{\min}(\boldsymbol{\gamma})$.

TABLE IV
STABILITY CRITERIA

Controller	α	$\lambda_{min}(T_D)$	$\lambda_{min}(\gamma_0)$	$\lambda_{min}(T_S)$	$\lambda_{min}(\gamma)$
DS	68.0360	128.400	1.0540	-	-
LSS, RSS	51.2735	-	-	74.6880	0.5931

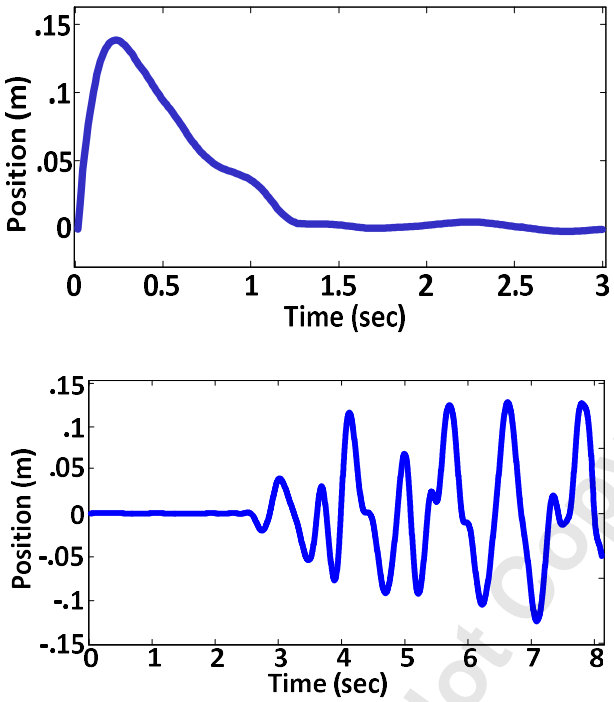

Figure 5. CoP when robot subjected to a single (above) and multiple (below) disturbance/s.

5.2 Walking Implementation

The simulation procedure involved the use of a series of dynamical models (Table I) of the robot with each one containing a complete representation of the actuator dynamics. Hence, three different controllers were designed for the DS, RSS and LSS models, whose switching was dictated by an FSM, whose structure is displayed in Fig. 6. Note that the LSS model is in essence a mirror-image of the RSS model and thus the mere rearrangement of the latter's gain matrices was sufficient for the construction of the former's gain matrices. Contrarily, the stiff lateral joints were controlled using a set of controllers whose PID gains were tuned by means of the conventional Routh array [43] technique, which revolves around the Routh criterion. There exists an equivalent tuning technique that utilises the Hurwitz criterion [43]. It was crucial that the controller would

be capable of displaying a satisfactory degree of tracking in the simulation, as this could indicate its potential tracking of walking trajectories when implemented on the robot. Although the walking trajectory generation technique considered the full 15 DOFs comprising the COMAN's lower body, it was oblivious to the presence of elastic elements in the sagittal joints. In order to ensure that the system remained stable during switching, it was crucial to not only rely upon the pertinent stability analyses, but rather to ensure that the voltage fluctuations occurring at the ideal controller switching instances were confined to evolving within the 0.8-1.2 Volt range. This specific range was selected using a systematic approach, by means of carrying out experiments that led to the determination of each joint's stiction-related deadband, in which the output would remain intact for a certain voltage value lying in the afore-stated range. Thus, the three gain sets associated with the three subsystems, were tuned in such a way so as to guarantee the prevention of voltage peaks when transitioning between the DS and SS models.

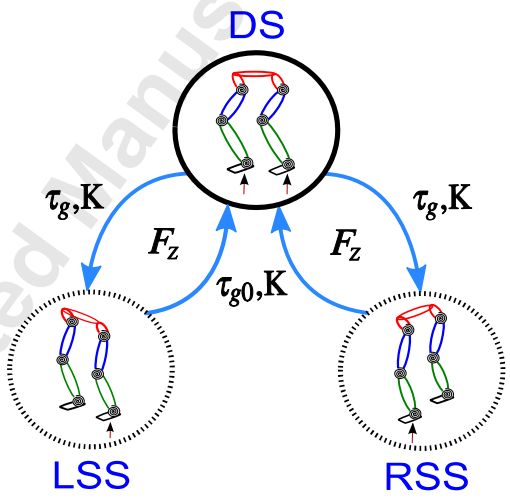

Figure 6. Walking controller finite state machine.

The controllers described were implemented on the COMAN, while the control scheme of Fig. 7 was used to ensure tracking of the desired walking trajectory that considered a walking step

length of 120 mm, coupled with a walking speed of 0.092 m/sec. Since the results displayed in Figs. 8-12 are associated with the PDD controller, the $\mathbf{G_{fg}}$ term in Fig. 7 corresponds to the generic feedforward term which either assumes the form $\mathbf{G_{fg}} = \mathbf{G_{ff}} = \mathbf{K_{j1}} + \mathbf{K_{m1}}$, or $\mathbf{G_{ff}} = \mathbf{K_{m1}}$, depending on which controller has been opted for.

Fig. 8 depicts the support and swing legs' simulated tracking of the walking trajectory, during which the controller switching occurred at time instants determined by the FT sensor feedback.

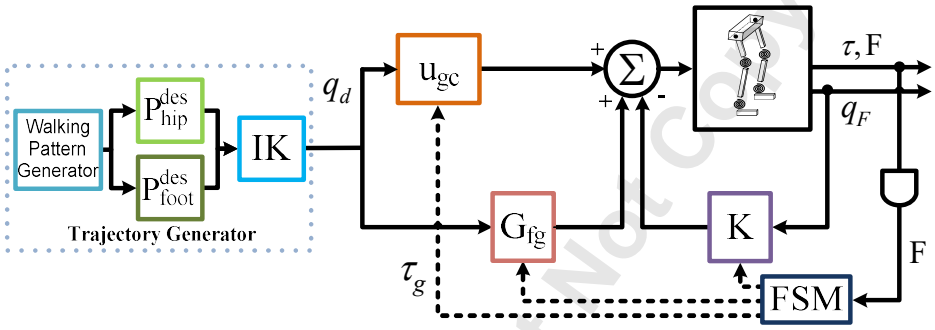

Figure 7. Walking strategy control loop block diagram including the FSM that modulates the feedforward and feedback terms.

In order to assess the robot's overall stability, an inspection of the joint tracking and Cartesian CoM position during the trajectory was required, as portrayed by Figs. 9 and 10. It is evident from these plots that the ankle demonstrates the poorest tracking capability of all the joints and this could be due to the cumbersome task of supporting the mass of the whole robot. Furthermore, the left and right foot and CoM positions depicted in Fig. 10 were computed using the link position data rather than the motor position data, thus accounting for the robot's oscillatory behaviour during motion, due to the passive joint elasticity. Fig. 11 portrays the GRFs measured on the right foot during walking, with the blue, red and yellow areas representing the DS, right SS and left SS respectively. It may be observed that the right-leg GRF magnitudes during the DS and left SS phases, are somewhat similar, and this is mainly attributed to imperfect touchdowns transpiring at the end of the single support phases. Additionally, Fig. 12 displays the various joint

control signal values produced during walking, which attest to the fact that the 24 Volt saturation voltage value has not been exceeded during the performance of the walking experiments.

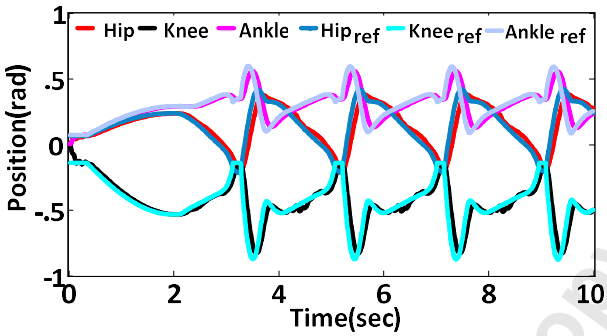

Figure 8. Walking trajectory tracking in simulation.

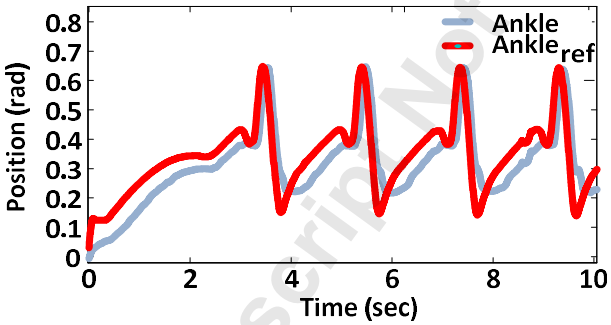

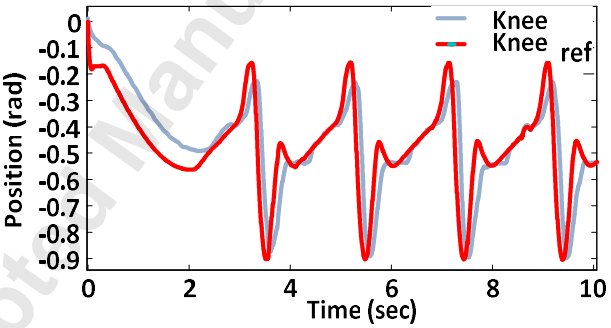

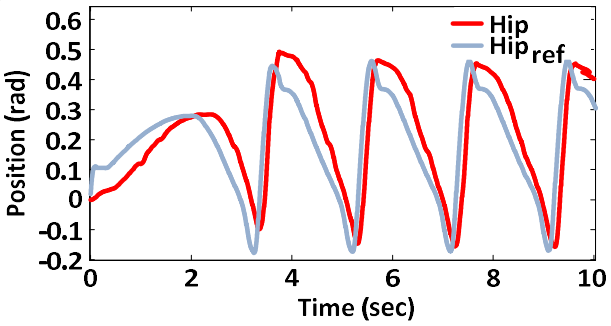

Figure 9. Ankle, knee and hip joint tracking.

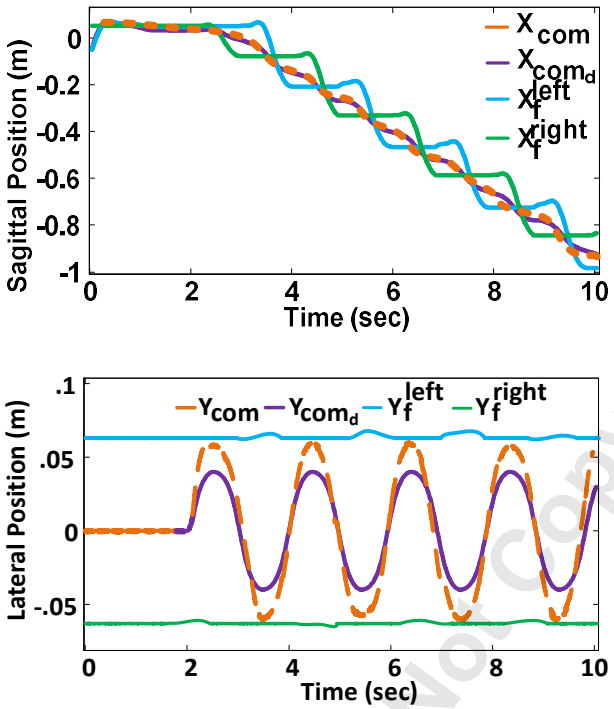

Figure 10. Cartesian X and Y CoM positions during walking.

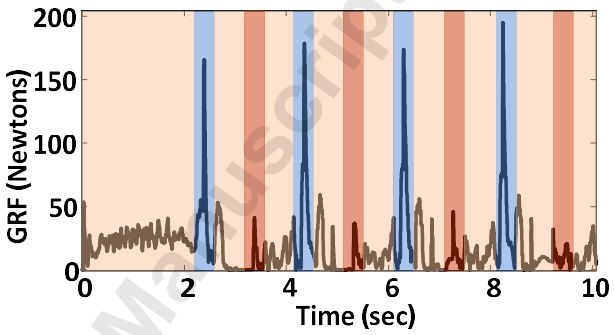

Figure 11. Right foot GRFs during walking.

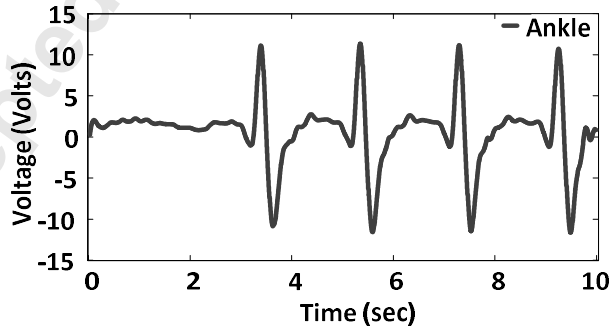

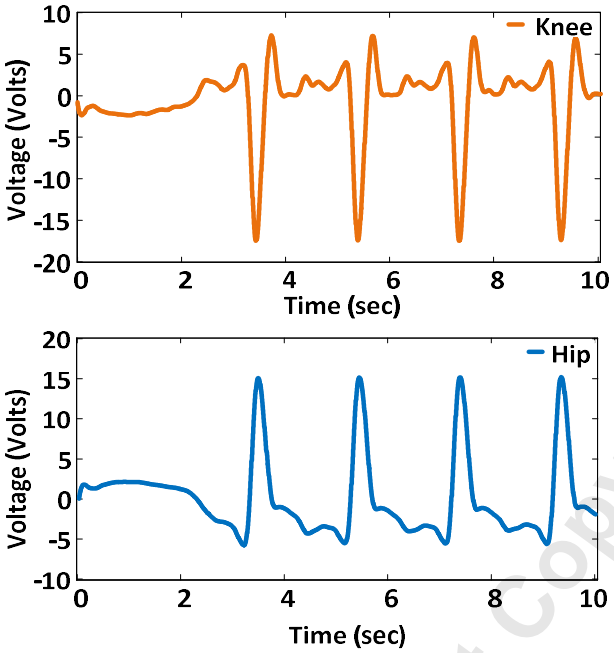

Figure 12. Ankle, knee and hip control voltages during walking.

The results indicate the controller's capability of endowing a passively compliant humanoid robot with a locomotory function, by utilizing a systematic model-based approach to gain tuning and feedforward control signal computation. The position tracking performance predicted in the simulations is congruous with that realised on the real robotic platform, as illustrated in Figs. 9 and 10. These results are encouraging in the sense that they corroborate the initial assertion that a control strategy accounting for both the link and motor feedback, could permit the execution of a walking trajectory that has been generated by considering a rigid robot model.

6. EXPERIMENTAL COMPARISON OF TWO NEW CONTROLLERS WITH EXISTING CONTROLLER

6.1 Simulation

In order to perform a fair comparison between the controllers introduced in the previous sections, and classical ones existing in the literature, the PD plus desired gravity compensation [14] controller has been selected, since it is an established and relevant control scheme. The

three techniques to be contrasted are displayed in Table V. It is reasonable to consider a comparison with a control scheme that deals directly with compliant joint robots, since a comparison with humanoid control methods pertaining to stiff robots would not only entail excessive time consumption in order to obtain decent experimental results, but would also lead to lengthening of the paper.

TABLE V
CONTROLLER SUMMARY

Controller	Description
A	PDD + desired gravity compensation
B	PPDD + desired gravity compensation
C	PD + desired gravity compensation

An impartial comparison necessitated the tuning of gains yielding the best possible performance (in terms of the joint bandwidth values) in each case, which is why controllers A and C were tuned by utilizing the Routh criterion, while controller B's tuning entailed modification of the Q and R penalties that ensured an attainment of the maximum joint bandwidths respecting the actuator saturation limits. The various controller link-side bandwidths, are summarized in Tables VI, VII and VIII. It is noteworthy that the LQR controller gains led to a satisfaction of the pertinent stability criteria, since $\lambda_{min}\left(\boldsymbol{\gamma}_{\mathbf{LQR_{DS}}}\right) = 1.64 \times 10^5$, while $\lambda_{min}\left(\boldsymbol{\gamma}_{\mathbf{LQR_{SS}}}\right) = 1.13 \times 10^5$, in addition to the bounds defined in Appendix A.

TABLE VI
PDD SCHEME LINK-SIDE BANDWIDTHS IN HERTZ

Controller	LA	LK	LH	RH	RK	RA
DS	1.86	1.84	3.70	3.70	1.84	1.86
RSS	2.56	2.37	1.98	1.77	1.54	1.41
LSS	1.41	1.54	1.77	1.98	2.37	2.56

TABLE VII
PPDD SCHEME LINK-SIDE BANDWIDTHS IN HERTZ

Controller	LA	LK	LH	RH	RK	RA
DS	1.96	1.89	3.72	3.72	1.89	1.96
RSS	2.71	2.58	2.13	1.97	1.81	1.66
LSS	1.66	1.81	1.97	2.13	2.58	2.71

TABLE VIII
PD SCHEME LINK-SIDE BANDWIDTHS IN HERTZ

Controller	LA	LK	LH	RH	RK	RA
DS	1.57	1.53	3.41	3.41	1.53	1.57
RSS	2.38	2.09	1.69	1.61	1.36	1.27
LSS	1.27	1.36	1.61	1.69	2.09	2.38

It is important to highlight the fact that the bandwidths were computed with reference to the link side instead of the motor side, since the motor bandwidths may be significantly greater than those of the links, although they only provide information related to what occurs before the elastic element, instead of describing the behaviour that transpires after the elastic element.

6.2 Walking Experiments

The walking experiments involved feeding a walking trajectory to Controllers A, B and C, while they had been implemented on the COMAN [12]. Ten walking trials were performed using each of the three controllers, amounting to 3 sets of 10 trials, where the average error for every set was computed independently. As was previously the case, the trajectories comprised walking step lengths of 120 mm, walking speeds of 0.092 m/sec, durations of 10 seconds, thus resulting in a total of 12 steps. Table IX lists the average tracking errors at the joint level, allowing one to observe the PPDD plus desired gravity compensation controller's superiority in terms of tracking. Fig. 13 portrays the Y-CoM tracking associated with the three controllers in a single plot, wherein it is demonstrated that the tracking differences are minute. Fig. 14 presents the sagittal CoM

tracking performance comparison in more detail, whereas Table X lists the mean and final error values, as well as the error gradient, for the three controllers. The error gradient could perhaps be viewed as the most important of the three values, since it describes the tendency of the error to increase as the trajectory evolves with time. In this light, it could again be stated that Controller C might be less reliable when desiring the execution of trajectories of longer duration. Another noteworthy value is the ratio of the final error to the desired X-CoM distance, whose values are 5.84%, 4.11% and 8.10% for Controllers A, B and C respectively. The error magnitudes in Fig. 14 increase over time, since they represent cumulative values described in Cartesian coordinates, while Fig. 15 exhibits the joint-space counterpart of Fig. 14.

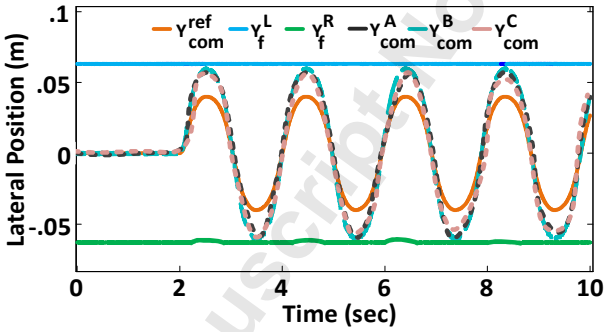

Figure 13. Y-CoM positions during walking (Controllers A, B, C).

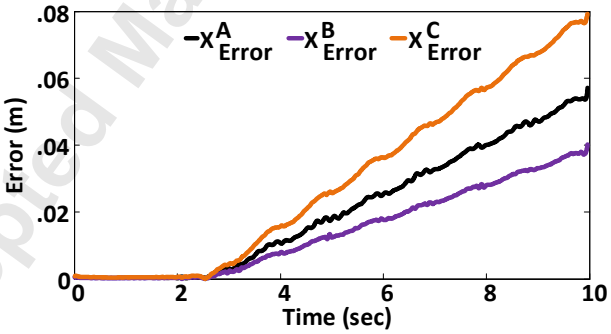

Figure 14. Absolute average X-CoM errors during walking.

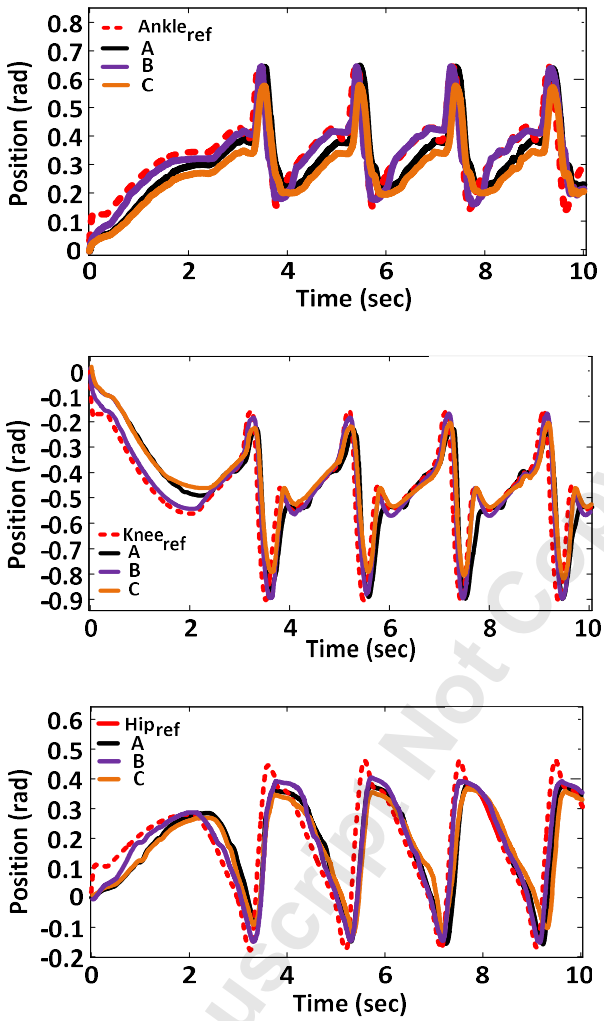

Figure 15. Ankle, knee and hip joint tracking during walking when using controllers A, B & C.

TABLE IX
AVERAGE JOINT TRACKING ERROR VALUES (RAD)

	Controller A	Controller B	Controller C
Ankle	0.0634	0.0509	0.0867
Knee	0.0488	0.0414	0.0594
Hip	0.0341	0.0311	0.0353

TABLE X
XCOM TRACKING ERROR VALUES DURING WALKING (MM)

	Controller A	Controller B	Controller C
Mean	33.0	26.6	53.1
Final	57.2	40.3	79.4
Gradient	5.7	4.0	7.9

It has been demonstrated that the augmentation of a compliant controller's dimension by the inclusion of full-state (PPDD) or even partial link-state (PDD) feedback, could generally yield improvements in terms of an SEA-powered bipedal robot's tracking performance, as regards its execution of walking trajectories. However, it is noteworthy that in addition to exhibiting the largest joint bandwidth values, the PPDD controller has practically demonstrated that it is capable of endowing the system with the most precise tracking. As a result, Fig. 14 attests to its ability to minimise the cumulative error that is accrued during the execution of a walking trajectory. Furthermore, the systematic, model-based means through which the PPDD controller's gains may be tuned, renders it the most favourable option owing to the method's repeatability, as compared to controllers A and C.

7 CONCLUSIONS

This paper has introduced PDD and PPDD control schemes combined with gravity compensation, which have led to the development of strategies that permitted COMAN to successfully execute walking trajectories. Three different dynamical models were utilized for the description of the various phases of the walking trajectory, resulting in three sets of gains, with the first control scheme employing motor position, motor velocity and link velocity feedback, and the second one exploiting full-state (PPDD) feedback. Moreover, each distinct PDD controller's stabilization capability was mathematically proven through the establishment of two conditions that were both shown to be satisfied by all the designed controllers. The stability results were also extended to tracking for both the PDD and PPDD schemes, in order to prove that the pertinent closed-loop systems were stable, even when provided with time-varying references, although this led to a

weaker stability condition as compared to that related to the set-point regulation results. Most importantly however, a switching condition was derived, whose fulfilment would ensure the stability of the full walking system by guaranteeing that the CoP would remain at a reasonable distance from the support polygon edges, thus preventing the occurrence of a fall. This implies that the system can switch between the different support stances in a stable fashion, so long as a set of sufficient conditions is satisfied. The experimental results allow us to deduce that the proposed approach is not only capable of balancing a compliant bipedal robot when subjected to disturbances while assuming a static configuration, but it also allows for the successful tracking of a desired dynamic walking trajectory. Furthermore, a comparison of the proposed schemes with a standard PD plus gravity compensation controller, has indicated the superior walking results obtained using the former methods, owing to the PPDD scheme's generation of an improved practical trajectory tracking performance, with 9%, 15% and 20% lower joint space error for the hip, knee and ankle respectively.

REFERENCES

[1] Vukobratovic, M., and Borovac, B., 2004, "Zero-moment point – Thirty Five Years of its Life," Int. J. Human. Rob., **1**(1), pp. 157-173.

[2] Sardain, P., and Bessonnet, G., 2004, "Forces Acting on a Biped Robot. Center of Pressure - Zero Moment Point," IEEE Trans. Syst., Man., Cyber., **34**(5), pp. 630-637.

[3] Hirai, K., Hirose, M., Haikawa, Y., and Takenaka, T., 1998, "The development of Honda humanoid robot," Proc. IEEE Int. Conf. Rob. and Aut., **2**, pp. 1321-1326.

[4] Pratt, J., and Pratt, G., 1998, "Intuitive control of a planar bipedal walking robot," Proc. IEEE Int. Conf. Rob. and Aut., pp. 2014-2021.

[5] Huang, Q., and Nakamura, Y., 2005, "Sensory reflex control for humanoid walking," IEEE Trans. Rob., **21**(5), pp. 977-984.

[6] Kajita, S., Morisawa, M., Miura, K., Nakaoka, S., Harada, K., Kaneko, K., Kanehiro, F., and Yokoi, K., 2006, "Biped walking stabilization based on linear inverted pendulum tracking," Proc. IEEE/RSJ Int. Conf. Intel. Rob. Syst., pp. 4489-4496.

[7] Sugimoto, N., and Morimoto, J., 2011, "Switching Multiple LQG Controllers Based on Bellman's Optimality Principle: Using Full-State Feedback to Control a Humanoid Robot," Proc. IEEE/RSJ Int. Conf. Intel. Rob. Syst., pp. 3185-3191.

[8] Spyrakos-Papastavridis, E., Medrano-Cerda, G., Tsagarakis, N., Dai, J., and Caldwell, D., 2013, "Gravity Compensation Control of Compliant Joint Systems with Multiple Drives," Proc. IEEE Int. Conf. Rob. and Aut., pp. 4960-4966.

[9] Spyrakos-Papastavridis, E., Medrano-Cerda, G., Tsagarakis, N., Dai, J., and Caldwell, D., 2013, "A compliant humanoid walking strategy based on the switching of state feedback gravity compensation controllers," Proc. IEEE/RSJ Int. Conf. Intel. Rob. Syst., pp. 3630-3636.

[10] Tsagarakis, N., Morfey, S., Medrano-Cerda, G., Li, Z., and Caldwell, D., 2013, "Compliant Humanoid COMAN: Optimal Joint Stiffness Tuning for Modal Frequency Control," Proc. IEEE Int. Conf. Rob. and Aut., pp. 673-678.

[11] Ugurlu, B., Tsagarakis, N., Spyrakos-Papastavridis, E., and Caldwell, D., 2011, "Compliant joint modification and real-time dynamic walking implementation on bipedal robot cCub," Proc. IEEE Int. Conf. Mech., pp. 833-838.

[12] Colasanto, L., Tsagarakis, N., Li, Z., and Caldwell, D., 2012, "Internal Model Control for Improving the Gait Tracking of a Compliant Humanoid Robot," Proc. IEEE/RSJ Int. Conf. Intel. Rob. Syst., pp. 5347-5352.

[13] Lim, B., Lee, M., Kim, J., Lee, J., Park, J., Seo, K., and Roh, K., 2012, "Control design to achieve dynamic walking on a bipedal robot with compliance," Proc. IEEE Int. Conf. Rob. and Aut., pp. 79-84.

[14] Tomei, P., 1991, "A Simple PD Controller for Robots with Elastic Joints," IEEE Trans. Aut. Cont., **36**(10), pp. 1208-1213.

[15] Kelly, R., and Santibánez, V., 1998, "Global Regulation of Elastic Joint Robots Based on Energy Shaping," IEEE Trans. Aut. Cont., **43**(10), pp. 1451-1456.

[16] Albu-Schäffer, A., and Hirzinger, G., 2001, "State feedback controller for flexible joint robots: A globally stable approach implemented on DLR's light-weight robots," Adv. Rob., **15**(8), pp. 799-814.

[17] De Luca, A., Siciliano, B., and Zollo, L., 2005, "PD Control with on-line gravity compensation for robots with elastic joints: Theory and Experiments," Automatica, **41**(10), pp. 1809-1819.

[18] Lanari, L., Sicard, P., and Wen, J., 1993, "Trajectory Tracking of Flexible Joint Robots: A Passivity Approach," Proc. Europ. Cont. Conf., **2**, pp. 886-891.

[19] Loria, A., and Ortega, R., 1995, "On tracking control of rigid and flexible joint robots," App. Math. and Comp. Sci, **5**(2), pp. 101-113.

[20] Tian, L., and Goldenberg, A., 1995, "Robust adaptive control of flexible joint robots with joint torque feedback," Proc. IEEE Int. Conf. Rob. and Aut., pp. 1229-1234.

[21] Choi, Y., Kim, D., and You, B., 2006, "On the walking control for humanoid robot based on the kinematic resolution of CoM Jacobian with embedded motion," Proc. IEEE Int. Conf. Rob. and Aut., pp. 2655-2660.

[22] Westervelt, E., Grizzle, J., and Koditschek, D., 2003, "Hybrid zero dynamics of planar biped walkers," IEEE Trans. Aut. Cont., **48**(1), pp. 42-56.

[23] Grizzle, J., Abba, G., and Plestan, F., 2001, "Asymptotically stable walking for biped robots: analysis via systems with impulse effects," IEEE Trans. Aut. Cont., **46**(1), pp. 51-64.

[24] Hyon, S., and Cheng, G., 2006, "Passivity-Based Full-Body Force Control for Humanoids and Application to Dynamic Balancing and Locomotion," Proc. IEEE/RSJ Int. Conf. Intel. Rob. Syst., pp. 4915-4922.

[25] Seo, K., Kim, J., and Roh, K., 2012, "Towards natural bipedal walking: Virtual gravity compensation and capture point control," Proc. IEEE/RSJ Int. Conf. Intel. Rob. Syst., pp. 4019-4026.

[26] Hyon, S., Hale, J., and Cheng, G., 2007, "Full-Body Compliant Human-Humanoid Interaction: Balancing in the Presence of Unknown External Forces," IEEE Trans. Rob., **23**(5), pp. 884-898.

[27] Schneiders, M., van der Molengraft, M., and Steinbuch, M., 2004, "Benefits of over-actuation in motion systems," Proc. Amer. Cont. Conf., pp. 505-510.

[28] Spong, M., 1987, "Modeling and Control of Elastic Joint Robots," J. Dyn. Sys., Meas., Control, **109**(4), pp. 310-319.

[29] Thelen, D., Anderson, F., and Delp, S., 2003, "Generating dynamics simulations of movement using computed muscle control," J. Biomech., **36**(3), pp. 321-328.

[30] Spong, M., 1989, "Adaptive Control of Flexible Joint Manipulators," Syst. Cont. Lett., **13**(1), pp. 15-21.

[31] Bacciotti, A., and Rosier, A., 2005, "Liapunov Functions and Stability in Control Theory," Comm. and Cont. Eng., **2**, pp. 112.

[32] Medrano-Cerda, G., Dallali, H., and Brown, M., 2012, "Control of a Compliant Humanoid Robot in Double Support Phase: a Geometric Approach," Int. J. Human. Rob., **9**(1), pp. 1250004-1/29.

[33] Dallali, H., Medrano-Cerda, G., and Brown, M., 2010, "A Comparison of Multivariable & Decentralized Control Strategies for Robust Humanoid Walking," Proc. UK Aut. Cont. Conf.

[34] Skogestad, and S., Postlethwaite, I., 2001, *Multivariable Feedback Control: Analysis and Design*, John Wiley & Sons.

[35] Ott, C., 2008, "Cartesian Impedance Control of Redundant and Flexible-Joint Robots," Springer Tracts in Advanced Robotics (STAR), **49**, pp. 116.

[36] Zhao, T., and Dai, J., 2003, "Dynamics and coupling actuation of elastic underactuated manipulators," J. Rob. Syst., **20**(3), pp. 135-146.

[37] Dai, J., and Zhao, T., 2002, "Stiffness characteristics and kinematics analysis of two-link elastic underactuated manipulators," J. Rob. Syst., **19**(4), pp. 169-176.

[38] Khalil, H., 2002, *Nonlinear Systems*, Prentice Hall.

[39] Xie, W., Wen, C., and Li, Z., 2001, "Input-to-state stabilization of switched nonlinear systems," IEEE Trans. Aut. Cont., **46**(7), pp. 1111-1116.

[40] Spyrakos-Papastavridis, E., Kashiri, N., Lee, J., Tsagarakis, N., and Caldwell, D., 2015, "Online Impedance Parameter Tuning for Compliant Biped Balancing," Proc. IEEE-RAS Int. Conf. Human. Rob., pp. 210-216.

[41] Spyrakos-Papastavridis, E., Perrin, N., Tsagarakis, N., Dai, J., and Caldwell, D., 2014, "Lyapunov stability margins for humanoid robot balancing," Proc. IEEE/RSJ Int. Conf. Intel. Rob. and Syst., pp. 945-951.

[42] Spyrakos-Papastavridis, E., Childs, P., and Tsagarakis, N., 2017, "Variable Impedance Walking using Time-Varying Lyapunov Stability Margins," Proc. IEEE-RAS Int. Conf. Human. Rob., pp. 318-323.

[43] Gopal, M., 1993, *Modern Control System Theory*, Wiley Eastern Limited.

[44] Brogliato, B., 2004, "Absolute stability and the Lagrange-Dirichlet theorem with monotone multivalued mappings," Syst. Cont. Lett., **51**(5), pp.343 -353.

APPENDIX A: THEORETICAL BOUNDS

The whole set of bounded terms considered in the stability analyses in Appendix B, in addition to terms that would be required in the DS analysis, may be viewed below. σ_{min} represents the minimum singular value.

$$\mu_{M_S} = inf\,\sigma_{min}\big(\mathbf{M}(\boldsymbol{q_E})\big), \mu_{M_D} = inf\,\sigma_{min}\big(\mathbf{M_0}(\boldsymbol{q_E})\big), \text{ where } \mathbf{M_0} = \begin{bmatrix} \mathbf{M_{J0}} & \mathbf{0} \\ \mathbf{0} & \mathbf{J} \end{bmatrix}.$$

$$\mu_{T_S} = \sigma_{min}(\mathbf{T_S}), \mu_{T_D} = \sigma_{min}(\mathbf{T_D}).$$

$$\mu_{\gamma} = \sigma_{min}(\boldsymbol{\gamma}), \mu_{\gamma_0} = \sigma_{min}(\boldsymbol{\gamma_0}).$$

$$\eta_{q_d} = sup\big\|\dot{\boldsymbol{q}}_{\boldsymbol{F_d}}(t)\big\|, \eta_{q_{dd}} = sup\big\|\ddot{\boldsymbol{q}}_{\boldsymbol{F_d}}(t)\big\|.$$

$$\eta_{D_S} = sup \sum_{i=1}^{n} \left\{\frac{\partial \mathbf{M}(\boldsymbol{q_F})}{\partial \boldsymbol{q}_{\boldsymbol{F_i}}}\right\}, \eta_{D\,d_S} = sup \sum_{i=1}^{n}\sum_{j=1}^{n} \left\{\frac{\partial^2 \mathbf{M}(\boldsymbol{q_F})}{\partial \boldsymbol{q}_{\boldsymbol{F_i}} \partial \boldsymbol{q}_{\boldsymbol{F_j}}}\right\}.$$

$$\eta_{D_D} = sup \sum_{i=1}^{n} \left\{\frac{\partial \mathbf{M}(\boldsymbol{q_F})}{\partial \boldsymbol{q}_{\boldsymbol{F_i}}}\right\}, \eta_{D\,d_D} = sup \sum_{i=1}^{n}\sum_{j=1}^{n} \left\{\frac{\partial^2 \mathbf{M_0}(\boldsymbol{q_F})}{\partial \boldsymbol{q}_{\boldsymbol{F_i}} \partial \boldsymbol{q}_{\boldsymbol{F_j}}}\right\}.$$

$$\eta_{DTOT_S} = \big\|\mathbf{D_{S_{TOT}}}\big\|, \eta_{DTOT_D} = \big\|\mathbf{D_{D_{TOT}}}\big\|.$$

$$\eta_{q_E} = sup\|\boldsymbol{q_E}(t)\|, \eta_{q_{Ed}} = sup\|\dot{\boldsymbol{q}}_{\boldsymbol{E}}(t)\|.$$

$$\xi_{M_S} = sup\|\mathbf{M}(\boldsymbol{q_F})\|, \xi_{M_D} = sup\|\mathbf{M_0}(\boldsymbol{q_F})\|.$$

$$\xi_{T_S} = \|\mathbf{T_S}\|, \xi_{T_D} = \|\mathbf{T_D}\|.$$

$$\xi_{\gamma} = \|\boldsymbol{\gamma}\|, \xi_{\gamma_0} = \|\boldsymbol{\gamma_0}\|.$$

In the above equations, the S and D subscripts denote the SS and DS configurations respectively.

APPENDIX B: SET-POINT REGULATION STABILITY ANALYSES

Proof 1: Using (1), (2), (7), (8), (10) and setting zero velocities and accelerations, gives the following expression (after some algebraic manipulations):

$$\mathbf{T_S}\begin{bmatrix}\boldsymbol{q}-\boldsymbol{q_d}\\ \boldsymbol{\theta}-\boldsymbol{\theta_d}\end{bmatrix}=\begin{bmatrix}\boldsymbol{\tau_g}(\boldsymbol{q})-\boldsymbol{\tau_g}(\boldsymbol{q_d})\\ \mathbf{0}\end{bmatrix}. \tag{28}$$

Letting $\boldsymbol{x}=[\boldsymbol{q}^{\boldsymbol{T}}\quad \boldsymbol{\theta}^{\boldsymbol{T}}]^{\boldsymbol{T}}$, $\boldsymbol{H}(\boldsymbol{x})=\boldsymbol{x_d}+\mathbf{T_S^{-1}}\boldsymbol{\tau}(\boldsymbol{x})$, where $\boldsymbol{\tau}(\boldsymbol{x})=\begin{bmatrix}\boldsymbol{\tau_g}(\boldsymbol{q})-\boldsymbol{\tau_g}(\boldsymbol{q_d})\\ \mathbf{0}\end{bmatrix}$, and using the contraction mapping theorem [38] in addition to equation (6), yields:

$$\|\boldsymbol{H}(\boldsymbol{x})-\boldsymbol{H}(\boldsymbol{y})\|\leq\lambda_{max}\left(\mathbf{T_S^{-1}}\right)\alpha\|\boldsymbol{x}-\boldsymbol{y}\|,$$

$$\therefore\quad \|\boldsymbol{H}(\boldsymbol{x})-\boldsymbol{H}(\boldsymbol{y})\|\leq\frac{\alpha}{\lambda_{min}(\mathbf{T_S})}\|\boldsymbol{x}-\boldsymbol{y}\|,$$

$\frac{\alpha}{\lambda_{min}(\mathbf{T_S})}<1$ is a sufficient condition to ensure that (28) has a unique solution. Hence, this gives:

$$\lambda_{\min}(\mathbf{T_S})>\alpha. \tag{29}$$

A crucial step in the construction of a suitable Lyapunov function is the selection of an appropriate auxiliary function. The following equation is therefore propounded, that can be seen to differ from similar functions presented in [14], [17]:

$$W_S=\frac{1}{2}\boldsymbol{q_E^T}\mathbf{T_S}\boldsymbol{q_E}+U_g(\boldsymbol{q})-U_g(\boldsymbol{q_d})+\boldsymbol{q_E^T}\begin{bmatrix}\boldsymbol{\tau_g}(\boldsymbol{q_d})\\ 0\end{bmatrix}, \tag{30}$$

where $\boldsymbol{q_F}=\begin{bmatrix}\boldsymbol{q}\\ \boldsymbol{\theta}\end{bmatrix}$, $\boldsymbol{q_{F_d}}=\begin{bmatrix}\boldsymbol{q_d}\\ \boldsymbol{\theta_d}\end{bmatrix}$, $\boldsymbol{q_E}=\left(\boldsymbol{q_F}-\boldsymbol{q_{F_d}}\right)$.

It can be demonstrated that (30) has a unique minimum at the equilibrium point $(\boldsymbol{q_d},\boldsymbol{\theta_d})$, through the following equation:

$$\nabla W_S(\boldsymbol{q},\boldsymbol{\theta})=\mathbf{T_S}\boldsymbol{q_E}+\begin{bmatrix}\boldsymbol{\tau_g}(\boldsymbol{q_d})-\boldsymbol{\tau_g}(\boldsymbol{q})\\ 0\end{bmatrix}=0. \tag{31}$$

From (31), one may conclude that the Hessian is positive definite and hence (30) has a unique minimum at $(\boldsymbol{q_d},\boldsymbol{\theta_d})$:

$$\nabla^2 W_S(\boldsymbol{q_d},\boldsymbol{\theta_d})=\mathbf{T_S}-\begin{bmatrix}\frac{\partial\boldsymbol{\tau_g}(\boldsymbol{q})}{\partial\boldsymbol{q}} & 0\\ 0 & 0\end{bmatrix}>0. \tag{32}$$

The following Lyapunov function formulation is therefore permitted:

$$V_S(\boldsymbol{q},\boldsymbol{\theta}) = \frac{1}{2}\dot{\boldsymbol{q}}_{\boldsymbol{F}}^{\boldsymbol{T}}\mathbf{M}(\boldsymbol{q})\dot{\boldsymbol{q}}_{\boldsymbol{F}} + W_S(\boldsymbol{q},\boldsymbol{\theta}) \geq 0, \tag{33}$$

where $\mathbf{M} = \begin{bmatrix}\mathbf{M_J} & \mathbf{0}\\ \mathbf{0} & \mathbf{J}\end{bmatrix}$. Obtaining the time derivative of the above function yields:

$$\dot{V}_S(\boldsymbol{q},\boldsymbol{\theta}) = \dot{\boldsymbol{q}}_{\boldsymbol{F}}^{\boldsymbol{T}}\mathbf{M}(\boldsymbol{q})\ddot{\boldsymbol{q}}_{\boldsymbol{F}} + \frac{1}{2}\dot{\boldsymbol{q}}_{\boldsymbol{F}}^{\boldsymbol{T}}\dot{\mathbf{M}}(\boldsymbol{q})\dot{\boldsymbol{q}}_{\boldsymbol{F}} - \dot{\boldsymbol{q}}_{\boldsymbol{F}}^{\boldsymbol{T}}\begin{bmatrix}\boldsymbol{\tau}_{\boldsymbol{g}}(\boldsymbol{q}) - \boldsymbol{\tau}_{\boldsymbol{g}}(\boldsymbol{q}_{\boldsymbol{d}})\\ 0\end{bmatrix} + \dot{\boldsymbol{q}}_{\boldsymbol{F}}^{\boldsymbol{T}}\mathbf{T_S}\boldsymbol{q}_{\boldsymbol{E}},$$

$$\dot{V}_S(\boldsymbol{q},\boldsymbol{\theta}) = \dot{\boldsymbol{q}}_{\boldsymbol{F}}^{\boldsymbol{T}}\begin{pmatrix}\begin{bmatrix}-\mathbf{C} & \mathbf{0}\\ \mathbf{0} & \mathbf{0}\end{bmatrix}\dot{\boldsymbol{q}}_{\boldsymbol{F}} + \frac{1}{2}\dot{\mathbf{M}}(\boldsymbol{q})\dot{\boldsymbol{q}}_{\boldsymbol{F}}\\ +\begin{bmatrix}\boldsymbol{\tau}_{\boldsymbol{g}}(\boldsymbol{q}_{\boldsymbol{d}}) - \boldsymbol{\tau}_{\boldsymbol{g}}(\boldsymbol{q})\\ 0\end{bmatrix} - \mathbf{T_S}\boldsymbol{q}_{\boldsymbol{E}}\\ -\begin{bmatrix}\mathbf{N} & \mathbf{0}\\ \mathbf{K_{VT}K_{j2}} & \mathbf{D} + \mathbf{K_{VT}K_{m2}}\end{bmatrix}\dot{\boldsymbol{q}}_{\boldsymbol{F}}\end{pmatrix} + \dot{\boldsymbol{q}}_{\boldsymbol{F}}^{\boldsymbol{T}}\mathbf{T_S}\boldsymbol{q}_{\boldsymbol{E}} + \dot{\boldsymbol{q}}_{\boldsymbol{F}}^{\boldsymbol{T}}\begin{bmatrix}\boldsymbol{\tau}_{\boldsymbol{g}}(\boldsymbol{q}) - \boldsymbol{\tau}_{\boldsymbol{g}}(\boldsymbol{q}_{\boldsymbol{d}})\\ 0\end{bmatrix},$$

$$\dot{V}_S(\boldsymbol{q},\boldsymbol{\theta}) = -\dot{\boldsymbol{q}}_{\boldsymbol{F}}^{\boldsymbol{T}}\begin{bmatrix}\mathbf{N} & \mathbf{0}\\ \mathbf{K_{VT}K_{j2}} & \mathbf{D} + \mathbf{K_{VT}K_{m2}}\end{bmatrix}\dot{\boldsymbol{q}}_{\boldsymbol{F}} \leq 0. \tag{34}$$

Since the matrix in (34) is not symmetric, proving its positive definiteness requires the performance of certain manipulations, commencing with a more succinct representation for brevity:

$$\begin{bmatrix}\mathbf{W} & \mathbf{X}\\ \mathbf{Y} & \mathbf{Z}\end{bmatrix} > 0. \tag{35}$$

An equivalent condition to (35) is

$$\begin{bmatrix}\dfrac{\mathbf{W} + \mathbf{W^T}}{\mathbf{2}} & \dfrac{(\mathbf{Y} + \mathbf{X})^{\mathbf{T}}}{\mathbf{2}}\\ \dfrac{\mathbf{Y} + \mathbf{X}}{\mathbf{2}} & \dfrac{\mathbf{Z} + \mathbf{Z^T}}{\mathbf{2}}\end{bmatrix} > 0. \tag{36}$$

Computing the Schur complement of (36) [38] and taking into account that $\mathbf{W}$, $\mathbf{X}$, $\mathbf{Y}$ and $\mathbf{Z}$ are diagonal matrices, the following equation arises:

$$\mathbf{W}\cdot\mathbf{Z} - \frac{(\mathbf{Y} + \mathbf{X})^2}{4} > 0. \tag{37}$$

Finally, setting $\mathbf{W} = \mathbf{N}$, $\mathbf{X} = 0$, $\mathbf{Y} = \mathbf{K_{VT}}\mathbf{K_{j2}}$, $\mathbf{Z} = \mathbf{D} + \mathbf{K_{VT}}\mathbf{K_{m2}}$, and since all these matrices are diagonal, one could arrive at equation (15) and the condition $\lambda_{min}(\boldsymbol{\gamma}) > 0$.

It may now be observed that $\dot{V}_S = 0$ if and only if $\dot{\boldsymbol{q}}_{\boldsymbol{F}} = 0$. By then substituting $\ddot{\boldsymbol{q}}_{\boldsymbol{F}} = \dot{\boldsymbol{q}}_{\boldsymbol{F}} = 0$ into the closed-loop equations (1), (2) and (7), one obtains:

$$\mathbf{P}(\boldsymbol{q} - \boldsymbol{\theta}) = \boldsymbol{\tau}_{\boldsymbol{g}}(\boldsymbol{q}), \tag{38}$$

$$\mathbf{P}(\boldsymbol{\theta} - \boldsymbol{q}) = \mathbf{K_{VT}}\big(\mathbf{K_{m1}}(\boldsymbol{q_d} - \boldsymbol{\theta}) + \boldsymbol{u_{gc}}\big). \tag{39}$$

By carrying out algebraic manipulations, it may be seen that (38) and (39) are equivalent to (28), that was previously shown to possess the unique equilibrium solution $[\boldsymbol{q_d^T} \quad \boldsymbol{\theta_d^T} \quad 0 \quad 0]^T$. Thus, it can be concluded that this is also the largest invariant subset among the set of states yielding $\dot{\boldsymbol{q}}_{\boldsymbol{F}} = 0$, in which case invocation of La Salle's theorem leads to the conclusion that the desired equilibrium point is globally asymptotically stable.

Proof 2: Using (3), (4), (11), (12), (14) and setting zero velocities and accelerations, gives the following expression (after some algebraic manipulations):

$$\mathbf{T_D}\begin{bmatrix} \boldsymbol{q_0} - \boldsymbol{q_{0_d}} \\ \boldsymbol{\theta} - \boldsymbol{\theta_d} \end{bmatrix} = \begin{bmatrix} \boldsymbol{\tau_{g0}}(\boldsymbol{q_0}) - \boldsymbol{\tau_{g0}}\big(\boldsymbol{q_{0_d}}\big) \\ \mathbf{0} \end{bmatrix}, \tag{40}$$

which possesses a unique solution if $\lambda_{min}(\mathbf{T_D}) > \alpha$.

The auxiliary function for this case would be the same as (30), with the only difference being the replacement of $\mathbf{T_S}$ with $\mathbf{T_D}$. The performance of calculations identical to those presented earlier, allows us to arrive at (34). Hence, the resulting Lyapunov function is similar to the one derived for the SS controller, although the matrices are of different dimensions. Setting $\ddot{\boldsymbol{q}}_{\boldsymbol{0_F}} = \dot{\boldsymbol{q}}_{\boldsymbol{0_F}} = 0$ in (3), (4) and (11), the following equations are acquired:

$$\mathbf{S_m^T P S_m} \boldsymbol{q} - \mathbf{S_m^T P} \boldsymbol{\theta} = \boldsymbol{\tau}_{g0}(\boldsymbol{q_0}), \tag{41}$$

$$\mathbf{P}\boldsymbol{\theta} - \mathbf{P S_m} \boldsymbol{q_0} = \mathbf{K_{VT}} \left(\mathbf{K_{m1_0}} \mathbf{S_m} \left(\boldsymbol{q}_{0_d} - \boldsymbol{\theta} \right) + \boldsymbol{u}_{gc_0} \right). \tag{42}$$

Following a similar approach to that used in Proof 1 and invoking LaSalle's theorem, allows us to conclude that the desired equilibrium point is globally asymptotically stable.

APPENDIX C: TRACKING STABILITY ANALYSIS

Since the stability analyses contained in Appendix B, are concerned solely with set-point regulation, it is now appropriate to demonstrate how these analyses could also be extended to trajectory tracking. It was mentioned earlier that the work seen in [18] has managed to prove local exponential stability of a class of flexible joint system controllers. Based on these results, a similar analysis is herein provided, which may be seen as an extension to these since a different form of feedback (i.e. link position and velocity feedback) is considered.

The stabilizing effect of the generic decentralized full-state (PPDD) feedback GC controller shall be proven, followed by a proof for the specific case in which the first and second order desired position derivative terms are eliminated from the feed-forward expression. Therefore, Theorem 3 shall serve as a stepping stone for the proof of the main theorems, namely Theorems 4 and 5. The generic feed-forward may be expressed as follows [18]:

$$\boldsymbol{V}_{m_{ff}} = \mathbf{K_{VT}^{-1}} \begin{bmatrix} \mathbf{0} \\ \boldsymbol{I} \end{bmatrix}^T \left(\mathbf{M} \ddot{\boldsymbol{q}}_{F_D} + \begin{bmatrix} \mathbf{C} & \mathbf{0} \\ \mathbf{0} & \mathbf{0} \end{bmatrix} \dot{\boldsymbol{q}}_{F_D} + \begin{bmatrix} \mathbf{N} & \mathbf{0} \\ \mathbf{0} & \mathbf{D} \end{bmatrix} \dot{\boldsymbol{q}}_{F_D} + \begin{bmatrix} \mathbf{P} & -\mathbf{P} \\ -\mathbf{P} & \mathbf{P} \end{bmatrix} \boldsymbol{q}_{F_D} - \begin{bmatrix} \boldsymbol{\tau}_g(\boldsymbol{q}) \\ \mathbf{0} \end{bmatrix} \right). \tag{43}$$

The full control signal is then given by:

$$\boldsymbol{V}_{m_T} = \mathbf{K_{m1}} (\boldsymbol{\theta_d} - \boldsymbol{\theta}) + \mathbf{K_{j1}} (\boldsymbol{q_d} - \boldsymbol{q}) + \mathbf{K_{m2}} \left(\dot{\boldsymbol{\theta}}_{\boldsymbol{d}} - \dot{\boldsymbol{\theta}} \right) + \mathbf{K_{j2}} (\dot{\boldsymbol{q}}_{\boldsymbol{d}} - \dot{\boldsymbol{q}}) + \boldsymbol{V}_{m_{ff}}, \tag{44}$$

where the link feedback gains $\mathbf{K_{j1}}$ and $\mathbf{K_{j2}}$ have been introduced, with respect to equation (43).

Theorem 3: Using the controller described by V_{m_T} on the LSS and RSS models, while assuming an adequately small $\eta_{q_d} = sup\left\|\dot{\boldsymbol{q}}_{\boldsymbol{F_d}}(t)\right\|$ value, then there exists an equilibrium point $\boldsymbol{q_d} - \boldsymbol{q} = \boldsymbol{\theta_d} - \boldsymbol{\theta} = 0$, that is locally exponentially stable.

Proof 3: The analysis leading to the proof of local exponential stability, is based on the definition of bounds on various system parameters that can be seen in Appendix A, while considering the following candidate Lyapunov function [18]:

$$V_{T1} = \frac{1}{2}\boldsymbol{q_E^T}\mathbf{T_{S_{LQR}}}\boldsymbol{q_E} + c\boldsymbol{q_E^T}\mathbf{M}\dot{\boldsymbol{q}}_{\boldsymbol{E}} + \frac{1}{2}\dot{\boldsymbol{q}}_{\boldsymbol{E}}^{\boldsymbol{T}}\mathbf{M}\dot{\boldsymbol{q}}_{\boldsymbol{E}} + \frac{c}{2}\boldsymbol{q_E^T}\mathbf{D_D}\boldsymbol{q_E}, \tag{45}$$

where 'c' is a positive constant and $\mathbf{D_D} = \begin{bmatrix} \mathbf{N} & \mathbf{0} \\ \mathbf{K_{VT}K_{j2}} & \mathbf{D} + \mathbf{K_{VT}K_{m2}} \end{bmatrix}$. A lengthy analysis using the bounds provided in Appendix A, allows one to prove that the system is exponentially stable.

Since the previous theorem relates solely to the generic PPDD terms, it is now appropriate to examine how this could be extended to the PPDD+GC controller presented earlier.

Proof 4: Consider the candidate Lyapunov function described by equation (45). Taking its time derivative along the trajectories of the closed-loop system, produces the following result:

$$\dot{V}_{TS} = -c\boldsymbol{q_E^T}\mathbf{T_{S_{LQR}}}\boldsymbol{q_E} + c\boldsymbol{q_E^T}\left(\dot{\mathbf{M}} - \begin{bmatrix} \mathbf{C} & \mathbf{0} \\ \mathbf{0} & \mathbf{0} \end{bmatrix}\right)\dot{\boldsymbol{q}}_{\boldsymbol{E}} - \dot{\boldsymbol{q}}_{\boldsymbol{E}}^{\boldsymbol{T}}(\mathbf{D_D} - c\mathbf{M})\dot{\boldsymbol{q}}_{\boldsymbol{E}} + \frac{c}{2}\dot{\boldsymbol{q}}_{\boldsymbol{E}}^{\boldsymbol{T}}\left(\mathbf{D_D} - \mathbf{D_D^T}\right)\boldsymbol{q_E}$$

$$+ \frac{\dot{\boldsymbol{q}}_{\boldsymbol{E}}^{\boldsymbol{T}}\left(\mathbf{T_{S_{LQR}}^T} - \mathbf{T_{S_{LQR}}}\right)\boldsymbol{q_E}}{2} + \left(c\boldsymbol{q_E^T} + \dot{\boldsymbol{q}}_{\boldsymbol{E}}^{\boldsymbol{T}}\right)\left(-\mathbf{M}\ddot{\mathbf{q}}_{\mathbf{F_d}} - \begin{bmatrix} \mathbf{C} + \mathbf{N} & \mathbf{0} \\ \mathbf{0} & \mathbf{0} \end{bmatrix}\dot{\boldsymbol{q}}_{\boldsymbol{F_d}} + \boldsymbol{\tau_g}(\boldsymbol{q_d}) - \boldsymbol{\tau_g}(\boldsymbol{q})\right). \tag{46}$$

Following a lengthy analysis, it can be demonstrated that V_{TS} is positive definite along the system's trajectories, thereby allowing one to conclude that the closed-loop system is Lagrange stable [44].

Proof 5: Following the steps outlined in Proofs 3 and 4, then the closed-loop system can be shown to be ISS.

Theorem 6: Using the controller described by equation (7) on the SS model, while assuming an adequately small $\eta_{q_d} = sup\left\|\dot{\boldsymbol{q}}_{\boldsymbol{F_d}}(t)\right\|$ value and that $\lambda_{min}(\boldsymbol{\gamma}) > 0$, then the closed-loop system is ISS.

Proof 6: Following the steps outlined in Proofs 3 and 4, having replaced the $\mathbf{T_{S_{LQR}}}$ with the $\mathbf{T_S}$ matrix, then the closed-loop system can be shown to be ISS.

Theorem 7: Using the controller described by equation (11) on the DS model, while assuming an adequately small $\eta_{q_d} = sup\left\|\dot{\boldsymbol{q}}_{\boldsymbol{F_d}}(t)\right\|$ value and that $\lambda_{min}(\boldsymbol{\gamma_0}) > 0$, then the closed-loop system is ISS.

Proof 7: Following the steps outlined in Proofs 3 and 4, having replaced the $\mathbf{T_{D_{LQR}}}$ with the $\mathbf{T_D}$ matrix, then the closed-loop system can be shown to be ISS.

Figure Captions List

Fig. 1 Figure 1. LSS (left), DS (centre) and RSS (right) models, and picture of COMAN's legs (rightmost).

Fig. 2 Simulated joint responses (0.3 radians step).

Fig. 3 Actual joint responses (0.3 radians step).

Fig. 4 Support polygon shape corresponding to DS stance.

Fig. 5 CoP when robot subjected to a single (above) and multiple (below) disturbance/s.

Fig. 6 Walking controller finite state machine.

Fig. 7 Walking strategy control loop block diagram including the FSM that modulates the feedforward and feedback terms.

Fig. 8 Walking trajectory tracking in simulation.

Fig. 9 Ankle, knee and hip joint tracking.

Fig. 10 Cartesian X and Y CoM positions during walking.

Fig. 11 Right foot GRFs during walking.

Fig. 12 Ankle, knee and hip control voltages during walking.

Fig. 13 Y-CoM positions during walking (Controllers A, B, C).

Fig. 14 Absolute average X-CoM errors during walking.

Fig. 15 Ankle, knee and hip joint tracking during walking when using controllers A, B & C.

Table Captions List

TABLE I DYNAMICAL MODELS

TABLE II LEG PARAMETER VALUES

TABLE III DAMPING PARAMETER VALUES

TABLE IV STABILITY CRITERIA

TABLE V CONTROLLER SUMMARY

TABLE VI PDD SCHEME LINK-SIDE BANDWIDTHS IN HERTZ

TABLE VII PPDD SCHEME LINK-SIDE BANDWIDTHS IN HERTZ

TABLE VIII PD SCHEME LINK-SIDE BANDWIDTHS IN HERTZ

TABLE IX AVERAGE JOINT TRACKING ERROR VALUES (RAD)

TABLE X XCOM TRACKING ERROR VALUES DURING WALKING (MM)